MŰEGYETEM 1782

Diploma Thesis

Electron Spin Resonance Spectroscopy on Boron-doped Diamond

Péter Szirmai

Thesis advisor: Ferenc Simon
University professor
Department of Physics
BME

Budapest University of Technology and Economics

BME
2013

Contents

A diplomatéma kiírása

Témavezető:

Neve:	Simon Ferenc
Tanszéke:	Fizika Tanszék
E-mail címe:	simon@esr.phy.bme.hu
Telefonszáma:	463-3816

Azonosító: DM-2012-39

Diplomatéma címe: Spintronikai alkalmazások motiválta új, szénalapú nanoanyagok szintézise és szilárdtest-spektroszkópiai vizsgálata

Melyik szakiránynak ajánlott? *"Kutatófizikus"*

A jelentkezővel szemben támasztott elvárások: Kitartó, szorgalmas munkavégzés, affinitás a kísérleti munka iránt, stabil elméleti alapok

Leírása: A spintronika a modern szilárdtestkutatás és anyagtudomány egyik legizgalmasabb területe. A spintronikai alkalmazásokhoz elengedhetetlen új és új anyagok előállítása és ezek vizsgálata a spin relaxációs idők nagyságának szempontjából. Utóbbit elektronspin-rezonancia spektroszkópia módszerrel valósítjuk meg. A spintronikai alkalmazások szempontjából felmerült anyagok a szén nanocsövek, a grafén és a bórral dópolt gyémánt. A jelentkező feladata i) alkáli atomokkal dópolt szén nanocsövek és grafén előállítása, ii) ezen anyagok mágneses és vezetési tulajdonságainak mérése ESR- és Raman-spektroszkópiai mérésekkel, iii) bórral dópolt gyémánton végzett hőmérsékletfüggő ESR-mérések elvégzése és ezek értelmezése. A jelentkező érdeklődésétől függően lehet az i-iii feladatok közül a hangsúlyt bizonyosakra helyezni a dolgozatban.

Önállósági nyilatkozat

Alulírott Szirmai Péter, a Budapesti Műszaki és Gazdaságtudományi Egyetem hallgatója kijelentem, hogy ezt a szakdolgozatot meg nem engedett segédeszközök nélkül, saját magam készítettem, és csak a megadott forrásokat használtam fel. Minden olyan szövegrészt, adatot, diagramot, ábrát, amelyet azonos értelemben más forrásból átvettem, egyértelműen, a forrás megadásával megjelöltem.

Budapest, 2013. június 3.

Szirmai Péter

Köszönetnyilvánítás

Hálával tartozom a szüleimnek, hogy szorgalmukkal megtanítottak a munka tiszteletére, és tanulmányaim alatt mindvégig támogattak.

Hálás vagyok a témavezetőmnek, Prof. Simon Ferencnek a többéves bizalmáért és lelkesítéséért. Szemléletes magyarázatai a szilárdtestfizika matematikai és fizikai felépítését természetességében mutatták be. Figyelme, alázatos munkavállalása és lankadatlan szorgalma követendő példa mindnyájunk számára.

Köszönettel tartozom Prof. Forró Lászlónak, hogy lehetővé tette Lausanne-ban a nyári gyakorlatokat, és lehetőséget biztosított a jelen dolgozat méréseire, továbbá Dr. Náfrádi Bálintnak a mérés során nyújtott segítségét. Prof. Thomas Pichlernek köszönöm, hogy biztosította az izgalmas nyári gyakorlatokat és a számos rövidebb látogatást a Bécsi Egyetemen.

Köszönet illeti Oliver A. Williamst a mintakészítésért, ill. Soumen Mandalt és Prof. Christopher Bäuerlét a transzportmérésekért és segítőkészségükért. Koltai Jánosnak köszönöm a sűrűségfunkcionál-elméleti számításokat.

Köszönöm Fábián Gábornak, Iván Dávidnak és Márkus Bencének segítségüket a közös munkában.

Köszönettel tartozom Vikinek, hogy az egyetemi évek alatt megértő támaszom és társam maradt. Hajni, Hanna, Bence, és Béci nyitottságukkal mindig új erőt adnak.

Acknowledgements

This thesis is dedicated to all my family for their constant support in my studies and trust in my plans.

I would like to express my sincere gratitude to my supervisor, Prof. Ferenc Simon for patiently and enthusiastically introducing me to solid-state physics. His way of thinking showed the mathematical and physical interpretations to be natural. His vivid atmosphere, unremitting energy, and prospective attitude is exemplary.

I am thankful for Prof. László Forró for the summer internships at EPFL, and to Dr. Bálint Náfrádi for his help in ESR measurements. I wish to express my sincere thanks to Prof. Thomas Pichler for the exciting summer internships and for several short visits in Vienna.

I am grateful to Oliver A. Williams for preparing the sample; to Soumen Mandal and Prof. Christopher Bäuerle for transport measurements and helpfulness; and to Dr. János Koltai for density functional theory calculations.

Financial support by the European Research Council Grant Nr. ERC-259374-Sylo is acknowledged.

Kivonat

Az elektron töltésének és spinjének manipulálásán alapuló spintronika az anyagtudományt és a szilárdtestfizikát leginkább egyesítő tudományterület. Habár a spintronikai alkalmazások első példái, a merevlemez-olvasófejek már fellelhetőek számítógépeinkben (2007-es fizikai Nobel-díj), a multidiszciplína számos jelentős jövőbeli alkalmazási lehetőséget kínál, amelyekkel kiválthatjuk elektronikai eszközeinket. A spintronikai eszközök előállításához három alapvető követelmény adható: spinpolarizált áram előállítása; a spin-relaxációs jellemzők ismerete; és a spin detektálása.

Az MSc diplomamunkámban egy nemrégiben felfedezett szupravezető, a bórral dópolt gyémánt (BDD) spinrelaxációs tulajdonságait vizsgálom elektronspin-rezonancia spektroszkópiával (ESR). Egy 6400 ppm bórral dópolt gyémánt ($T_\mathrm{c} = 3.8$ K) mintán azonosítom a vezetési elektronok ESR-jelét (CESR) normál állapotban.

A dolgozat röviden összefoglalja a BDD szokatlan fizikai tulajdonságait, köztük a szigetelő-szupravezető átmenetből eredő jellemzőit. A mágneses rezonancia és a vezetési elektronspin-rezonancia elméletét fenomenologikusan tárgyalom.

A CESR jellemzőit azonosítom a BDD-ben: (i) az ESR-intenzitás karakterisztikusan eltér az $1/T$-jellegű Curie-hőmérsékletfüggéstől; (ii) az állapotsűrűség összhangban van fotoemissziós mérésekkel; (iii) a vonalszélesség enyhén növekszik a hőmérséklettel, teljesítve a fémek spinrelaxációjának Elliott-Yafet-elméletét. Az empirikus Elliott-Yafet-reláció Beuneu-Monod-ábráját alkalmazva anomális összefüggést állapítok meg a g-faktor eltolódás, a CESR vonalszélesség és az ellenállás között, amely szokatlanul nagy spinrelaxációs időre (τ_s) utal a bórral dópolt gyémántban.

A bemutatott eredmények jelentős része nemrégiben megjelent a Phys. Rev. B folyóiratban [1].

Abstract

Spintronics, i.e., the manipulation of spin and charge degrees of freedom of electron creates the closest link between materials science and solid-state physics. The earliest examples of spintronic applications are present in our computers as read heads of hard drives (Nobel Prize in Physics in 2007). Nevertheless, this multidisciplinary field possesses an immense potential to replace all electronic devices by their spintronic counterpart. To make useful devices, three fundamental issues are to be adressed: polarization of a spin ensemble; spin-relaxation properties; and detection of the spin.

In my Master's thesis, I investigate the spin-relaxation properties of a recently discovered superconductor, boron-doped diamond (BDD) using electron spin resonance spectroscopy (ESR). The electron spin resonance of itinerant electrons (CESR) is observed in a 6400 ppm boron-doped sample ($T_\mathrm{c} = 3.8$ K) in the normal state.

This work gives a short summary of the unusual physical properties of BDD, especially those arising from the insulator-superconductor transition. The theory of magnetic resonance and that of the CESR are phenomenologically discussed.

The benchmarks of CESR are identified in BDD: (i) the ESR signal intensity characteristically differs from the Curie (i.e., $1/T$) temperature dependence; (ii) the density of states matches the value based on photoemission spectroscopy measurements; and (iii) the ESR linewidth displays a slight increase with increasing temperature in accordance with Elliott-Yafet theory of spin relaxation. Using the Beuneu-Monod plot of the empirical Elliott-Yafet relation, an anomalous relation is found between the g-factor shift, the CESR linewidth, and the resistivity. The latter result indicates an unexpectedly large spin-relaxation time (τ_s).

Results presented herein were recently published in Phys. Rev. B [1].

Chapter 1

Introduction and motivations

Limitations of today's electronics might be overcome with using the spin degree of freedom, which is the core principle in the field of spintronics[1]. For spintronic applications, an effective way of spin polarization, spin injection, control on spin relaxation, and error-free spin detection is needed [2].

To generate spin-polarized current and to detect it, the re-discovered spin Hall effect (SHE) has become a standard tool within a decade [3, 4]. The SHE, which originates from the spin-orbit coupling, deflects the electrons perpendicular to the current in a spin-dependent way, and inversely, spin current induces a perpendicular electric current [5].

To effectively manipulate information in spintronic devices, the spin-relaxation time, τ_s, should be in the range of 10ns . . . 1 μs. An often cited concept is that "pure materials made of light elements" might approach this limit [6]. (Nevertheless, the recent observation of unexpectedly low τ_s in graphene [7] contradicted this rule of thumb.)

The diversity of carbon materials gives rise to a remarkable range of applications. Diamond, the three-dimensional allotrope of carbon is widely used in the industry due to its superlative properties, such as, e.g., the mechanical stability and the large mobility [8]. It has been proposed that diamond is appropriate for quantum information processing applications [9, 10] and for nano-electromechanical (NEMS) devices [11]. The weak spin-orbit coupling of carbon makes it a viable candidate for future spintronic applications.

Boron-doped diamond (BDD) is an example of Mott's metal above the threshold boron concentration $n_c = 4 - 5 \cdot 10^{20}$ cm^{-3}. The experimental discovery of superconductivity in BDD in 2004 [12] came as a major surprise to the research community working on diamond. It has been proven that superconductivity arises from the lightly hole-doped

---

[1] The term was coined by S. A. Wolf in 1996, as a name for a DARPA initiative for novel magnetic materials and devices.

diamond bands [13], and an increase of the superconducting critical temperature can be achieved by additional doping [14]. As BDD might be relevant for future spintronics, a spin-relaxation study is required. Herein, I study the electron spin resonance in BDD to determine τ_s.

In this thesis, I present the theoretical background and results of my work. In Chapter 2, I introduce the basic concepts of superconductivity and the studied material, boron-doped diamond, and I give a short review on the experimental and theoretical investigation of spin dynamics in metals. In Chapter 3, the characterization measurements of BDD samples and the description of the experimental setup are presented. Chapter 4 provides the ESR measurement results and the discussion. The thesis concludes with a short summary in Chapter 5.

Chapter 2

Theoretical background

In my Master's project, I studied the spin dynamics of superconducting boron-doped diamond. To establish these investigations, a theoretical overview is required on the extraordinary properties of boron-doped diamond, with special emphasis on superconductivity, and the spin relaxation in metals.

2.1 Superconductivity

Here, I will recapitulate the striking features and basic theories of superconductors. The elementary properties of superconductors are the following: (i) superconducting materials show zero electrical DC resistance below the superconducting critical temperature (T_c); (ii) below T_c and below a critical value of the applied magnetic field, a superconductor behaves as a perfect diamagnet regarding its response to the magnetic field (Meissner-effect); (iii) below T_c a superconducting gap [$2\Delta(T)$] occurs around the Fermi level; (iv) a supercurrent appears between two separated superconductors (Josephson-effect) [15].
By 1950, experimentally several of these unique properties were known, however, the Ginzburg-Landau theory could only give a phenomenological description. The first microscopic theory was provided in the seminal paper of Bardeen, Cooper, and Schrieffer (BCS) [16]. Therein, an electron-gas was considered, where the electrons interact via exchange of virtual phonons, i.e., electrons pair up to form bound states of *Cooper pairs.* The BCS theory simplified the attractive interaction of electrons near the Fermi energy by an effective interaction V, e.g., it was neglected that the phonon interaction is retarded in time. The BCS theory yields an experimentally relevant relation between T_c and the

density of states, $D(E_\mathrm{F})$:

$$T_\mathrm{c} = 0.85\,\theta_\mathrm{D} \exp\left(-\frac{1}{D(E_\mathrm{F})V}\right), \tag{2.1}$$

where θ_D is the Debye temperature. This equation is only valid in the weak-coupling limit of the electron-phonon coupling: $1 \gg D(E_\mathrm{F})V = \lambda$. The energy gap at 0 K, $\Delta(0)$, is connected to T_c via

$$\frac{\Delta(0)}{k_\mathrm{B}T_\mathrm{c}} = 1.76, \tag{2.2}$$

where k_B is the Boltzmann constant.

Due to ignoring the details of the electron-phonon interaction, the interaction V was replaced by more realistic potentials. In the framework of the Eliashberg theory [17], the modern expression of the electron-phonon coupling constant reads

$$\lambda = 2\int_0^\infty \mathrm{d}\Omega \frac{g(\Omega)F(\Omega)}{\Omega} = 2\int_0^\infty \mathrm{d}\Omega \frac{\alpha^2 F(\Omega)}{\Omega}. \tag{2.3}$$

Herein, $g(\Omega)$ is the electron-phonon matrix element, $F(\Omega)$ is the phonon density of states, and $\alpha^2F(\Omega)$ is the Eliashberg spectral function of electron-phonon scattering.

To take into account the screened Coulomb repulsion, a dimensionless quantity, μ is introduced. The Coulomb pseudopotential is renormalized due to retardation, and reads as follows

$$\mu^* = \frac{\mu}{1 + \mu \ln\left(\frac{E_\mathrm{F}}{k_\mathrm{B}\theta_\mathrm{D}}\right)}, \tag{2.4}$$

where E_F is the Fermi energy.

Via numerical solutions of the Eliashberg equations, McMillan [18] could reproduce T_c in most cases using the expression:

$$T_\mathrm{c} = \frac{\theta_\mathrm{D}}{1.45} \exp\left\{-\frac{1.04(1+\lambda)}{\lambda - \mu^*(1+\lambda)}\right\}. \tag{2.5}$$

Superconductors can be classified according to two basic criteria. The existence of one or two critical magnetic fields defines *Type-I* and *Type-II* superconductors, respectively. In the case of Type-II superconductivity, magnetic field can penetrate in form of flux lines (vorteces). Based on the validity of the BCS theory, superconducting materials are *conventional* or *unconventional* [15].

2.2 Boron-doped diamond

The superlative properties of diamond make it irreplaceable in several industrial applications. The appearance of man-made diamond on the diamond market and in scientific

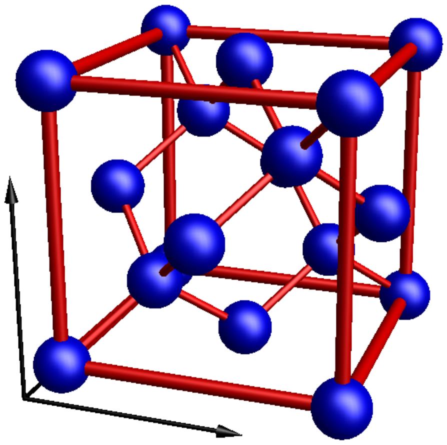

Figure 2.1: The crystal lattice of diamond [19].

Figure 2.2: Chemical vapour deposition (CVD) synthetic diamond is used for a wide range of high-technology applications [20].

laboratories was therefore an important leap to unravel its exceptional behaviour. Herein, I will give a short summary of the synthesis methods of this material, and I will discuss the insulator-metal transition in its derivative, boron-doped diamond.

2.2.1 Synthesis and basic properties

The sp^3-bonded allotrope of carbon, diamond, is a metastable crystal at ambient pressure and temperature. Whereas thermodynamically the sp^2 bonds are more stable, the activation barrier separating the sp^2-bonded graphite and diamond is large enough to prevent the transformation. Diamond crystallizes in a variation of face-centered cubic structure (see Fig. 2.1), the so-called diamond lattice. It consists of two interpenetrating face-centered cubic Bravais lattices, displaced along the body diagonal of the cubic cell by one quarter the length of the diagonal [21].

Pure diamond is colorless and transparent. However, due to different substitutional impurities and defects, natural diamond can be found in various colours. The strong covalent bonding explains that diamond is the hardest material in the nature. It has large tensile strength, excellent thermal conductivity, and large Debye temperature (θ_D). Unlike graphite, it is a large, indirect band-gap (5.5 eV) insulator [22].

The excellent thermal conductivity, the large breakdown field and the large electron and hole mobility would support its application in electronic devices. In order to build diamond-based integrated (or even spintronic) devices, one needs to overcome several difficulties. The rarity of natural diamond requires a facile, high-yield synthesis method, with which both *p*- and *n*-type doping can be achieved [22]. Below, I will show that the former two issues has already been resolved. Although the lack of *n*-type doping was a serious obstacle to applications, successful *n*-type doping with shallow donors has recently been demonstrated [23].

The production of man-made diamond (see Figure 2.2) was attempted as early as 1880 [24]. The first, reproducible method, the so-called high-pressure high-temperature (HPHT) method was adapted in 1955 by General Electrics Company [25]. Although commercially the low-pressure methods would have been more attracting, the chemical vapour deposition method (CVD) was invented as late as the 1980s.

High-pressure high-temperature method

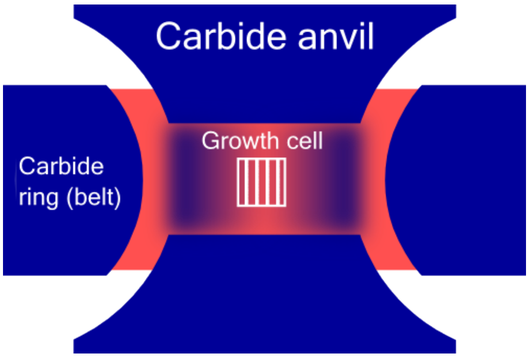

Figure 2.3: The belt press design for HPHT production of synthetic diamond [26].

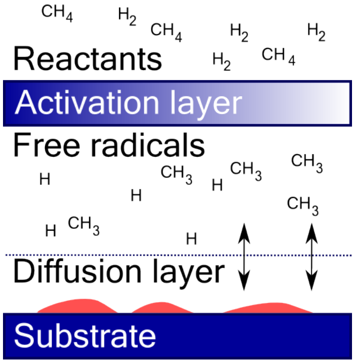

Figure 2.4: Schematic description of the CVD method [22].

The HPHT process mimics the natural diamond growth due to geophysical processes. A typical setup of the HPHT approach is shown in Fig. 2.3. The so-called *belt* press design involves huge hydraulic press at high temperature on the starting high-purity carbon material with anvils (8-9 GPa at 2500-2800 K for 5 s). In between a ring-shaped structure confines the radial press [27]. The starting materials are, in general, graphite discs.

Due to the relatively low price, the HPHT method remains widely used in the cutting and abrasive industry. In addition, it is used in jewelry for enhancing the properties of natural diamond.

Chemical vapour deposition

The success of the CVD process in the 1980s rekindled the attention to man-made diamond [28]. In Fig. 2.4, the schema of the CVD process is shown. The process relies on decomposing carbon-containing gas molecules (*reactants*), such as methane to *free radicals*, and depositing diamond on a *substrate* [20]. The presence of hydrogen plays an important role, as it can remove non-diamond carbon and it can terminate a part of the carbon ‘dangling’ bonds [22]. As a side effect, hydrogen is present in different complexes in diamond films. A well-known example of this is trans-polyacetylene [29]. The ionization of gases (*activation*) in the reaction chamber can be achieved by microwave power, a hot filament or by other means [20].

In contrast to the HPHT approach, CVD is preferred in reasearch laboratories, as this procedure yields significantly lower impurity concentrations. Due to recent improvements [20, 30], longer carrier lifetime and higher drift mobility were observed in CVD diamond than in “high-quality” natural diamond.

The cost of the CVD method can be reduced by growing nanocrystalline diamond, instead of bulk single crystals [31]. Several properties of nano-structured diamond are similar to the bulk material, except for the lower carrier mobility and thermal conductivity [32, 33]. Nanocrystalline diamond possesses a number of advantages, such as, e.g., the applicability as nano-electromechanical system devices [11], bio-markers [34] or as single photon sources [35], and the possibility to grow on several alternative substrates [36]. To achieve successful growth, a nucleation enhancement step is required on substrates.

2.2.2 Conduction properties

The recent interest in boron-doped diamond (BDD) was initiated by the remarkable discovery of superconductivity in BDD prepared by the HPHT method in 2004 [12]. In the following, I will briefly review the insulator-metal transition upon boron doping, the superconducting properties of BDD, and the transport properties in the framework of weak localization.

Insulator-metal transition

In the HPHT approach, substitutional p-type boron doping can be achieved by adding B_4C to graphite. Boron doping with the CVD method relies on adding gaseous trimethylboron to the methane as a reactant.

When the boron concentration is increased above a critical concentration n_c, the insulator behaviour changes to metallic. Using secondary ion mass spectrometry (SIMS), the critical concentration is found to be $n_c \approx 4-5\cdot 10^{20}$ cm^{-3} [37], largely depending on the synthesis procedure.

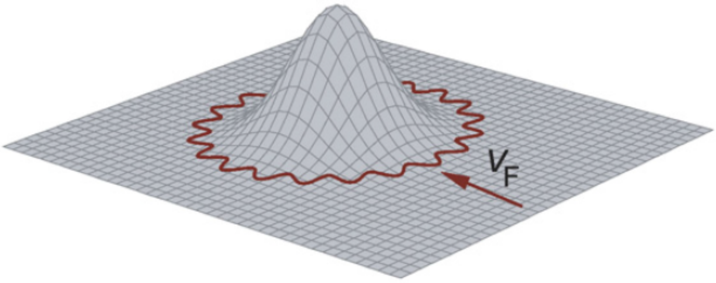

Figure 2.5: Illustration of the weak localization. A stable localized electron-wave interference pattern, called weakly localized orbit circumvents a large scale potential fluctuation [40].

The Mott transition [38] is an insulator-to-metal transition, where a doped semiconductor becomes a metal. It takes place when the concentration of the randomly distributed boron reaches n_c, and the boron-related states overlap. This is directly related to the Bohr radius, which reads

$$a_\mathrm{B} = \frac{\varepsilon a_0}{m^*}, \tag{2.6}$$

where ε is the dielectric constant, a_0 is the Bohr radius in vacuum, and m^* is the effective mass in units of m_e. The critical concentration is expected at $a_\mathrm{B} n_\mathrm{c}^{1/3} = 0.26$. With the usual values ($\varepsilon = 5.7$ and $m^* = 0.74$), this simple relation gives $n_\mathrm{c} = 6 \cdot 10^{20}$ cm^{-3} [14, 39], which is in reasonable agreement with the experimental value of n_c.

Normal state

Concerning BDD, one of the most important discussions was on the nature of itineracy above the critical boron concentration. It was found theoretically that metallic behaviour is either due to the lightly hole-doped diamond bands [41] or due to the acceptor bands [42]. An angle-resolved photoemission spectroscopy (ARPES) study [13, 43] showed the validity of the former prediction, i.e., that conduction (and thus superconductivity) is intrinsic to BDD and that the conduction band is derived from the valence band of diamond.

Below a certain temperature, the normal-state resistivity of boron-doped diamond increases slowly when the temperature is reduced. At this temperature, the inelastic and the elastic mean free paths are the same order of magnitude. The essence of this effect, the so-called weak localization (see Figure 2.5) is the constructive quantum interference of electron waves split and elastically scattered by potential fluctuations. The weak localization in BDD arises from electron-phonon scattering [14], and it is pronounced and well-known in nanocrystalline diamond [44].

The second-order, insulator-to-metal transition in BDD can be described by two critical exponents, ν and η. The former relates the correlation length (ξ_{loc}) to n_{B} as $\xi_{\mathrm{loc}} \propto 1/\left|n_{\mathrm{B}} - n_{\mathrm{C}}\right|^{\nu}$. η connects the energy and length scales of the system: $E \propto 1/L^{\eta}$. Experimentally, $\eta \approx 3$ and $\nu = 1$ were obtained in agreement with the theory [45]. The scaling behaviour is expected to reduce the density of states as $D(E_{\mathrm{F}}) \propto \left|n_{\mathrm{B}} - n_{\mathrm{C}}\right|^{\nu(3-\eta)}$.

Superconducting state

As pointed out in Sec. 2.2.1, samples produced by the HPHT method show high impurity concentration. This might suggest that superconducting boron ($T_{\mathrm{c}} = 6$ K at 175 GPa) [46] is responsible for the observed superconductivity in BDD. The doubt was first raised by Ekimov *et al.* [12] but the opposite pressure dependence of T_{c} in boron and in BDD contradicted the assumption. Later on, a high-resolution transmission electron microscopy (HRTEM) study [47] showed evidence that amorphous boron causes superconductivity and it was claimed that intrinsic superconductivity in BDD was unlikely. The controversy was resolved when superconductivity was confirmed in CVD prepared materials [48]. For materials produced with the microwave plasma enhanced CVD process, a significant orientation dependence was found, and T_{c} up to 11 K was measured in (111) oriented samples [49].

Although it was expected that the T_{c} in BDD would be increased by additional boron doping [50, 51], it turned out that boron tends to form boron pairs [52] and hydrogen in the CVD process effectively passivates the boron acceptors, leading to B-H complexes [53]. In addition, the enhancement of T_{c} at lower doping levels is explained by the vicinity of the insulator-metal transition [14].

Several reports [54, 55, 56] confirmed that the BCS approach is valid in BDD. In this respect, the relatively high T_{c} for a disordered semiconductor-derived material is due to the energetic phonons in diamond, which is a stiff material. The type-II superconductivity (confirmed, e.g., in Ref. [57]) originates from the strong coupling of phonons to the holes in the diamond bands. The three-dimensional metallic bands couple to three zone-centre optical phonon modes, in contrast to MgB_2, where the metallic bands are two-dimensional and couple to two optical phonon modes. Despite a very large electron-phonon coupling potential V for diamond [58], the three-dimensional nature reduces its density of states compared to MgB_2. Therefore, the electron-phonon coupling λ is 0.4-0.5 [50], whereas it is $\lambda \approx 1$ in MgB_2, which results in significantly lower critical temperatures in BDD [22].

Even if superconductivity in doped semiconductors is an intriguing issue for theory [56, 59], until 2004, it was only observed for GeTe, SnTe and for doped SrTiO_3. Following the results of Ekimov *et al.* [12], boron-doped silicon ($T_c \approx 0.35$ K [60]) and silicon carbide ($T_c \approx 1.4$ K [61]) were also found to be superconducting.

2.3 Spin dynamics in metals

In the following, I present experimental techniques and theoretical background of spin dynamics in metals. This leads us to the discussion of spin dynamics in BDD. I present transport- and spectroscopy-based spin-relaxation techniques, especially the Hanle spin-precession experiment and the conduction electron spin resonance. Finally, I will discuss the Elliott-Yafet theory, i.e., the relevant spin relaxation mechanism in metals with inversion symmetry.

2.3.1 Spin transport

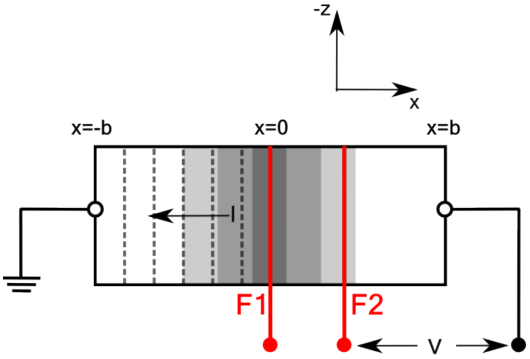

Figure 2.6: Schematic view of non-local quasi one-dimensional Johnson-Silsbee scheme. F1 and F2 are ferromagnetic contacts with magnetization in the $x-z$ plane; dotted lines are the equipotentials; gray shading shows the nonequilibrium spin-polarized electrons [2].

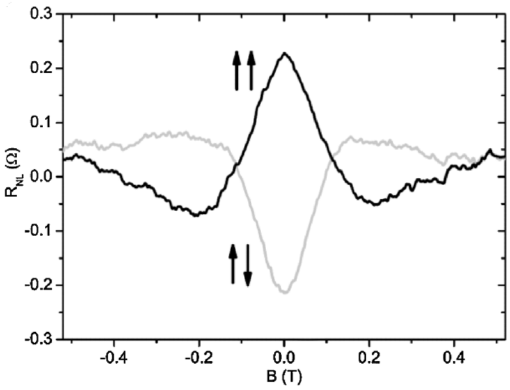

Figure 2.7: Hanle spin-precession experiment in graphene in case of parallel (↑↑, black curve) and antiparallel (↑↓, gray curve) magnetizations of the spin-injector and spin-detector electrodes [62].

To calculate τ_s, it is plausible to measure time and space correlations in magnetization. E.g. transmission electron spin resonance (TESR) was successfully applied by Jánossy [63] to determine the propagation of nonequilibrium magnetization of excited electrons in paramagnetic metals.

In electrical spin-injection experiments, the Johnson-Silsbee scheme [64, 65] is used, as depicted in the non-local geometry in Fig. 2.6. Therein, the F1 contact injects I current toward the grounded left end of the wire, leading to a linear voltage drop from F1 to the ground. F1 is ferromagnetic, thus, the spin-polarized electrons diffuse in the $\pm x$ direction, with a spin-diffusion length of $\delta_{\text{spin}} = v_{\text{F}}\sqrt{\tau\tau_s}$, where v_{F} is the Fermi velocity and τ is the momentum relaxation time. As F2 is ferromagnetic as well, electrons with parallel spin to the magnetization of F2 cause a spin-dependent voltage from F2 to the right end at $x = b$. Hence, if the $x = L_x$ position of F2 is varied, the exponential decay of this voltage could yield δ_{spin} and τ_s.

However, it is a major difficulty to reproduce these devices with different L_x values. Instead, the zero frequency analogue of the TESR, the so-called Hanle spin-precession method is employed. There, a magnetic field is applied transverse to the orientation of the injected spins. The electrons precess under the influence of the field, which provokes a phase coherence loss for large enough fields. In general, Hanle data (shown in Fig. 2.7) are fit to a mixture of absorptive and dispersive contributions. These fits to the magnetic field dependence provide information on the spin polarization and the spin-diffusion length [66]. The Hanle method was recently demonstrated in mesoscopic devices [67] and in graphene [7].

2.3.2 Electron spin resonance

Since its discovery in 1944 [68], electron spin resonance (ESR) spectroscopy has been proven to be a convenient contactless technique in studying the magnetic properties of biological and chemical systems. In solid-state physics, ESR became an important method in identifying the ground state of strongly correlated electron systems [69]. E.g. ESR characterization was key for the synthesis of phase pure AC_{60} (A=K, Rb, Cs) [70] fulleride polymer. This technique was also utilized to examine the spin-relaxation properties of the conventional superconductor with the highest T_{c}, MgB_2 [71, 72].

A free electron possesses a spin $\mathbf{S}$ resulting in a magnetic moment of

$$\boldsymbol{\mu} = -\frac{g_e\mu_{\text{B}}}{\hbar}\mathbf{S}. \tag{2.7}$$

Herein, $g_e = 2.0023(1)$ is the free electron g-factor, $\mu_{\text{B}} = 9.27(4)\cdot 10^{-24}$ J/T is the Bohr magneton, and $\hbar$ is the Planck constant. In the absence of a magnetic field, the energy levels of the two spin quantum states with $m_s = \pm 1/2$ quantum numbers are degenerate. If a $\mathbf{B_0} = B_0 \cdot \mathbf{k}$ external magnetic field is applied to the electron, the degeneracy is lifted. The energy difference is $\Delta E = E_{+1/2} - E_{-1/2} = g_e\mu_{\text{B}}B_0$, in agreement with classical electrodynamics.

In a solid-state, the energy splitting of the electron leads to the so-called Zeeman Hamiltonian

$$\mathcal{H}_{\text{ext}} = -\boldsymbol{\mu} \cdot \mathbf{B_0} = g_J \mu_{\text{B}} \mathbf{J} \cdot \mathbf{B_0}. \tag{2.8}$$

g_J is the so-called Landé g-factor, $\mathbf{J} = \mathbf{L} + \mathbf{S}$ is the total angular momentum. Hence, the energy splitting reads as

$$\Delta E = g_J \mu_{\text{B}} J_z B_0. \tag{2.9}$$

Applying the Ehrenfest theorem for the time dependence of the total angular momentum [73]

$$\frac{\mathrm{d}\langle \mathbf{J} \rangle}{\mathrm{d}t} = \frac{i}{\hbar} \langle [\mathcal{H}_{\text{ext}}, \mathbf{J}] \rangle = \gamma \langle \mathbf{J} \rangle \times \mathbf{B_0}, \tag{2.10}$$

where the gyromagnetic ratio $\gamma = 2\pi \cdot 28.0$ GHz/T is introduced, and $\langle . \rangle$ indicates the quantum mechanical expectation value. The equation of motion is similar to the classical case: the $\mathbf{B_0}$ magnetic field produces a torque on the angular momentum, and this results in a Larmor precession around $\mathbf{B_0}$ with $\omega_{\text{L}} = \gamma B_0$ frequency.

In an ESR experiment, a transition is induced through switching on an alternating magnetic field along the x axis: $B_x = B_{x0} \cos \omega t$. This linearly polarized B_x can be analyzed by breaking it into two rotating components. Close to the resonance, the component which rotates opposite to the precession of the moment, may be neglected. Without loss in generality, we assume that the clockwise rotating $\mathbf{B_1} = B_1 \left[\mathbf{i} \cos(\omega t) - \mathbf{j} \sin(\omega t) \right]$ ($B_1 = B_{x0}/\sqrt{2}$) induces the transition. In the laboratory frame, Eq. (2.10) for the $\gamma \mathbf{J} = \boldsymbol{\mu}$ magnetic moment can be rewritten as

$$\frac{\mathrm{d} \langle \boldsymbol{\mu} \rangle}{\mathrm{d}t} = \langle \boldsymbol{\mu} \rangle \times \gamma \left[\mathbf{B_0} + \mathbf{B_1} \right]. \tag{2.11}$$

In the frame whose x-axis rotates along $\mathbf{B_1}$, it becomes

$$\frac{\partial \langle \boldsymbol{\mu} \rangle}{\partial t} = \langle \boldsymbol{\mu} \rangle \times \underbrace{\left[\mathbf{k}(\gamma B_0 - \omega) + \mathbf{i} \gamma B_1 \right]}_{\mathbf{B}_{\text{eff}}}. \tag{2.12}$$

Clearly, the classical equation is now valid for the $\mathbf{B}_{\text{eff}}$ effective magnetic field. The resonance condition is satisfied with $\gamma B_0 - \omega \approx 0$, i.e., if the frequency of the perturbing field is equal to the Larmor frequency: $\omega \approx \omega_{\text{L}}$.

In the rotating frame, near the resonance, the $\boldsymbol{\mu}$ magnetic moment rotates around the x axis. The magnetic potential energy is, therefore, periodically returned.

Eq. (2.12) discusses the spin-flip without friction, which led to a precession around an effective magnetic field in the rotating frame. The Bloch-equations [74] consider an exponential relaxation in the laboratory frame for $\mathbf{M} = \boldsymbol{\mu}/V$ magnetization components in the material:

$$\begin{aligned}\frac{\mathrm{d}M_z}{\mathrm{d}t} &= \gamma(\mathbf{M}\times\mathbf{B})_z + \frac{M_0 - M_z}{T_1}\\ \frac{\mathrm{d}M_x}{\mathrm{d}t} &= \gamma(\mathbf{M}\times\mathbf{B})_x - \frac{M_x}{T_2}\\ \frac{\mathrm{d}M_y}{\mathrm{d}t} &= \gamma(\mathbf{M}\times\mathbf{B})_y - \frac{M_y}{T_2}.\end{aligned} \tag{2.13}$$

$\mathbf{B}$ is the effective magnetic field, M_0 is the equilibrium magnetization through the z-axis, T_1 is the spin-lattice, and T_2 is the spin-spin relaxation time. The longitudinal T_1 and the transversal T_2 relaxation times are, in general, different, as the former describes an energy transfer to a reservoir.

The Bloch-equations can be solved in the rotating frame [73], where the solution for the in-plane component reads as

$$\begin{aligned}M_x' &= \frac{\chi_0\omega_0}{\mu_0}T_2\frac{(\omega_0-\omega)T_2}{1+(\omega-\omega_0)^2T_2^2}B_1\\ M_y' &= \frac{\chi_0\omega_0}{\mu_0}T_2\frac{1}{1+(\omega_0-\omega)^2T_2^2}B_1.\end{aligned} \tag{2.14}$$

Herein, $'$ indicates the solutions in the rotating frame, $\chi_0 = \mu_0 M_0/B_0$ is the static volume susceptibility, and $\omega_0 = \gamma B_0$ is the resonance frequency.

Regarding M_x' and M_y' as components of a complex function, the solution in the standing reference frame reads

$$M_x^C = M_x' e^{i\omega t} + M_y' e^{i\omega t} e^{i\pi/2}. \tag{2.15}$$

Similarly, the complex function of the perturbing magnetic field is defined as

$$B_x^C = B_{x,0}e^{i\omega t}. \tag{2.16}$$

Using Eq. (2.15) and Eq. (2.16), the linear response function, i.e., the volume magnetic susceptibility reads

$$\chi = \mu_0\frac{M_x^C}{B_x^C} = \chi' - i\chi''. \tag{2.17}$$

(χ is also called the dynamic susceptibility.) χ' and χ'' are the elastic (or dispersive) and dissipative responses of the system, respectively. These are connected by the Kramers-Kronig theorem.

Spin susceptibilities

For a material in thermal equilibrium, the Zeeman splitting yields to slight difference in spin populations due to the Boltzmann law. This population difference is measured by the spin susceptibility of the material, which is proportional to the ESR intensity (see Sec. 4.1.1).

Since a non-interacting spin system is a canonical ensemble, with its energy levels defined in Eq. (2.9), the free energy reads

$$F = -N k_{\mathrm{B}} T \ln \left(\sum_n e^{-\beta E_n} \right), \tag{2.18}$$

where N is the number of atoms and $\beta = 1/k_{\mathrm{B}}T$. The component of the volume magnetization along the field is

$$M = -\frac{1}{V}\frac{\partial F}{\partial B} = \frac{N}{V} g_J \mu_{\mathrm{B}} J B_J \left(\beta g_J \mu_{\mathrm{B}} J B_0 \right), \tag{2.19}$$

where $B_J(x)$ is the Brillouin function. For low magnetic fields, the small-x expansion of the Brillouin function is: $B_J(x) \approx \frac{J+1}{J} x/3$. For the Curie spin susceptibility, this yields

$$\chi_0(\mathrm{Curie}) = \mu_0 \frac{N}{V} \frac{g_J^2 \mu_{\mathrm{B}}^2 J(J+1)}{3 k_{\mathrm{B}} T}, \tag{2.20}$$

where μ_0 is the vacuum permeability. In Mn^{2+}, the angular momentum is quenched [73], and J is replaced by S. In a solid-state, the Landé g-factor, g_J, is substituted by the g-factor, which takes into account the local field in the sample [75, 76].

In case of conducting samples, the free-electron gas model is valid. In this case, the electrons obey the Fermi-Dirac distribution

$$f(\varepsilon) = \frac{1}{e^{\beta(\varepsilon - \mu)} + 1}. \tag{2.21}$$

Herein, ε is the energy and μ is the chemical potential. When a B_0 magnetic field is applied, the energy gain (loss) due to the parallel (anti-parallel) spin of the electron is $\frac{1}{2} g \mu_{\mathrm{B}} B_0$. This energy difference leads to a surplus of the parallel spins, i.e., paramagnetic linear response of the metal. Due to the nearly stepwise Fermi-Dirac distribution, the Pauli spin susceptibility of the conducting samples is proportional to the electronic density of states at the Fermi level, $D(E_{\mathrm{F}})$:

$$\chi_0(\mathrm{Pauli}) = \mu_0 \frac{g^2}{4} \mu_{\mathrm{B}}^2 D(E_{\mathrm{F}}) \frac{1}{V_c}. \tag{2.22}$$

V_c is the volume of the unit cell [76]. A dimensional analysis shows that when $D(E_{\mathrm{F}})$ is measured in units of $1/(\mathrm{energy} \cdot \mathrm{unit})$, χ is dimensionless in SI units, as required.

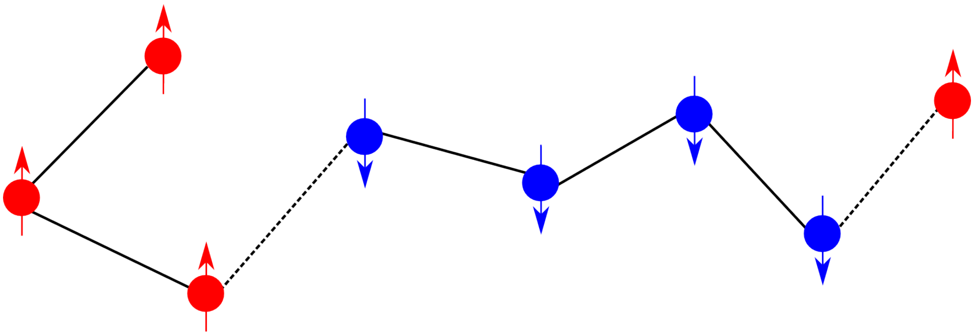

Figure 2.8: Schematic of the Elliott-Yafet spin-relaxation mechanism during spin transport [77].

2.3.3 Elliott-Yafet spin-relaxation mechanism

The spin-orbit coupling in atomic physics enters into the Hamiltonian from the $1/c^2$-expansion of the relativistic Dirac equation. In central potential, this approach gives

$$\mathcal{H}_{\mathrm{SO}} = \frac{ke^2}{2m_e^2 r^3 c^2}\mathbf{L}\cdot\mathbf{S}, \tag{2.23}$$

where $k = 1/4\pi\varepsilon_0$ is the Coulomb constant, m_e is the free electron mass, and c is the speed of light. Eq. (2.23) expresses that the moving electron experiences a magnetic field in its rest frame that arises from the Lorentz transformation of the static electric field. Elliott [79] showed that the presence of spin-orbit interaction ($\mathcal{H}_{\mathrm{SO}}$) leads to Bloch states which are an admixture of the spin-up $|\uparrow\rangle$ and spin-down $|\downarrow\rangle$ states with $\mathbf{k}$ lattice momentum:

$$\begin{aligned} \Psi_{\mathbf{k},\uparrow}(\mathbf{r}) &= \left[a_{\mathbf{k}}(\mathbf{r})\,|\uparrow\rangle + b_{\mathbf{k}}(\mathbf{r})\,|\downarrow\rangle\right] \quad e^{i\mathbf{k}\mathbf{r}} \\ \Psi_{\mathbf{k},\downarrow}(\mathbf{r}) &= \left[a^*_{-\mathbf{k}}(\mathbf{r})\,|\downarrow\rangle + b^*_{-\mathbf{k}}(\mathbf{r})\,|\uparrow\rangle\right] \quad e^{i\mathbf{k}\mathbf{r}}. \end{aligned} \tag{2.24}$$

Herein a and b are the lattice periodic coefficients written with the explicit dependence with the radius $\mathbf{r}$. The two degenerate Bloch states can be called $\Psi_{\mathbf{k},\uparrow}(\mathbf{r})$ and $\Psi_{\mathbf{k},\downarrow}(\mathbf{r})$, as $a \approx 1$ and b is

$$|b| = \frac{\lambda}{\Delta E} \ll 1 \tag{2.25}$$

as shown by perturbation theory. λ is the amplitude of the matrix element of $\mathcal{H}_{\mathrm{SO}}$, and ΔE is the energy distance between the band state in question and the state in the nearest band with the same transformation properties. The g-factor shift, $\Delta g = g - g_e$ can be estimated by taking the matrix element of l_z on the unperturbed function, so that Δg is at the order of $|b|$:

$$\Delta g = \alpha_1 \frac{\lambda}{\Delta E}, \tag{2.26}$$

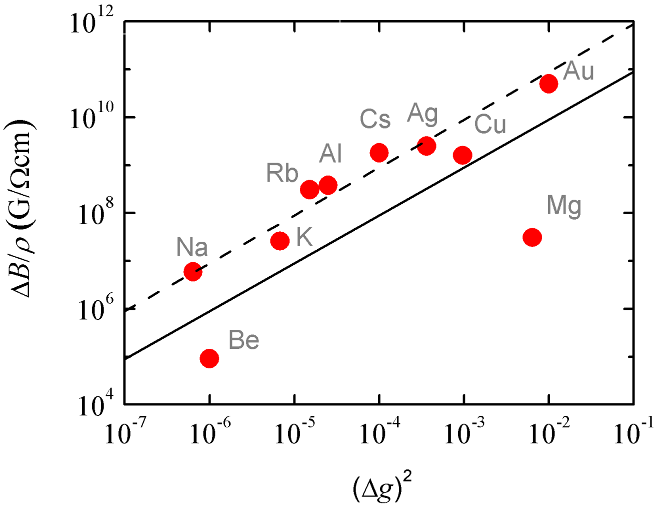

Figure 2.9: The original Beuneu-Monod plot showing the connection between $(\Delta g)^2$ and the ration of the ESR linewidth and resistivity for pure metals $\Delta B/\varrho$. Solid line and dashed curve correspond to $\alpha_1/\alpha_2^2 = 1$ and $\alpha_1/\alpha_2^2 = 10$, respectively [78].

where α_1 is a constant over unity.

To give an estimate on τ_s (in metals $\tau_s = T_1 = T_2$), the Elliott [79] and Yafet [80] relations will be discussed. The Elliott relation expresses that the momentum scattering is proportional to the spin-flip scattering. With the momentum scattering interaction $\mathcal{H}_{\text{int}}$, the wave functions of Eq. (2.24) yield

$$\left|\langle\Psi_{\mathbf{k},\uparrow}\left|\mathcal{H}_{\text{int}}\right|\Psi_{\mathbf{k'},\downarrow}\rangle\right|^2 = |b|^2 \cdot \left|\langle\Psi_{\mathbf{k},\uparrow}\left|\mathcal{H}_{\text{int}}\right|\Psi_{\mathbf{k'},\uparrow}\rangle\right|. \tag{2.27}$$

Combining the g-factor shift and τ_s, the Elliott relation reads

$$\frac{1}{\tau_s} = \alpha_2 \left|\frac{a_{\mathbf{k}}}{b_{\mathbf{k}}}\right|^2 = \alpha_2 \left(\frac{\Delta g}{\alpha_1}\right)^2 \frac{1}{\tau}, \tag{2.28}$$

where τ is the momentum relaxation time. The estimated τ/τ_s ratio is dependent on the scattering mechanism, that is, whether it stems from impurities, boundaries or phonons. Within the Drude model, the conductivity reads

$$\sigma = \frac{1}{\varrho} = \frac{ne^2\tau}{m^*} = \varepsilon_0\omega_{\text{pl}}^2\tau, \tag{2.29}$$

where n is the electron density, m^* is the effective mass, and ω_{pl} is the plasma (angular) frequency. Substituting the ESR linewidth $\Delta B = 1/\gamma T_1$ and Eq. (2.29) into Eq. (2.28), it yields [81]

$$\Delta B = \frac{\varepsilon_0\omega_{\text{pl}}^2}{\gamma}\frac{\alpha_1}{\alpha_2^2}(\Delta g)^2 \cdot \varrho. \tag{2.30}$$

This expression corresponds to the more general Yafet relation

$$\frac{1}{T_1(T)} \propto |b|^2\, \varrho(T), \tag{2.31}$$

which was justified over a large temperature range even when the temperature dependence of the resistivity is non-linear, i.e., well below the Debye temperature [2].

The Elliott-Yafet relation (shown schematically in Fig. 2.8) in Eq. (2.30) combines three independent empirical parameters, ΔB, Δg, and ϱ, i.e., it is a benchmark of spin-relaxation experiments in novel metals. Beuneu and Monod [78, 82] verified its validity for elemental metals. There, the variation of ω_{pl} from metal to metal was neglected and the linear scaling was established between $\Delta B/\varrho$ and $(\Delta g)^2$. Figure 2.9 depicts the Beuneu-Monod plot for pure metals. $\alpha_{1,2}$ may vary between $1 \ldots 10$, and the best fit was found for 10^{11} G/Ωcm. The linear scaling of the Elliott-Yafet relation occurs mostly for monovalent materials and notable exceptions are Be and Mg for which the so-called "hot-spot" model was invoked by Fabian and Das Sarma to explain the data [83]. The hot-spot model recognizes that spin relaxation is enhanced for particular points of the Fermi surface. Given that the spin lifetime is much larger than the momentum lifetime, an electron wanders over large portions of the Fermi surface before spin relaxation occurs, i.e., the hot spots dominate the spin relaxation. This effect is pronounced for metals where the Fermi surface strongly deviates from a sphere.

2.4 CESR signal in metals

ESR is most commonly used for the observation of localized paramagnetic spins (often termed as electron paramagnetic resonance). Therefore care is required for the identification of ESR signal of conduction electrons in metals. Even a small amount of impurity could hinder the observation of the latter. Notable examples of CESR identifications from the recent past are the discovery of CESR in Rb_3C_{60} [84], in RbC_{60} [70], in MgB_2 [71], and in carbon nanotubes [85].

Herein, we give the benchmarks of observing an ESR signal originating from the itinerant electrons in a metal. In the order of importance [69]:

(a) The value of the measured spin susceptibility should match the Pauli spin susceptibility, which is related to the density of states.

(b) The temperature dependence of the signal intensity should be characteristically different from the Curie dependence ($\chi(\mathrm{Curie}) \propto 1/T$).

(c) For a metal with inversion symmetry, the linewidth should increase with increasing temperature following the Elliott-Yafet relaxation mechanism [79, 86].

(d) The g-factor shift and the ESR line-width should obey the Elliott-Yafet relation.

Chapter 3

Experimental techniques

The bulk properties of BDD as a disordered metal were measured using X-band electron spin resonance technique. This chapter starts out with a review of the characterization measurements performed on the BDD samples. Transport measurements were performed to examine the conduction properties of BDD. Its light scattering properties were investigated by Raman spectroscopy using visible excitations. Later on, I will introduce the ESR spectrometer I used.

3.1 Samples and their characterization

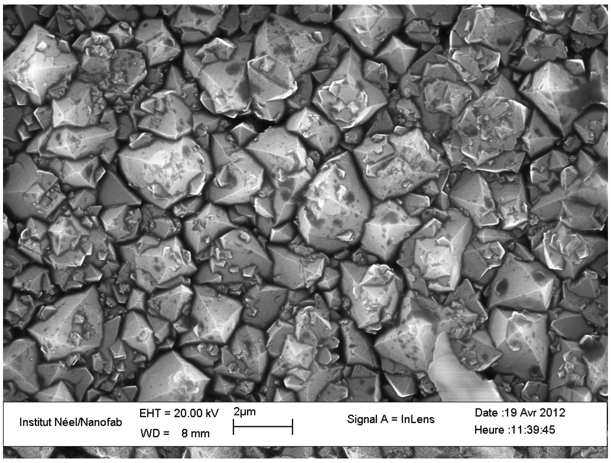

Figure 3.1: Scanning Electron Microscope (SEM) image of the surface of the sample prepared by MPCVD method, consisting of grains of typically 3 μm size.

To prepare our samples[1], diamond nucleation was initiated by immersion of clean

---

[1] The samples were prepared by Oliver A. Williams.

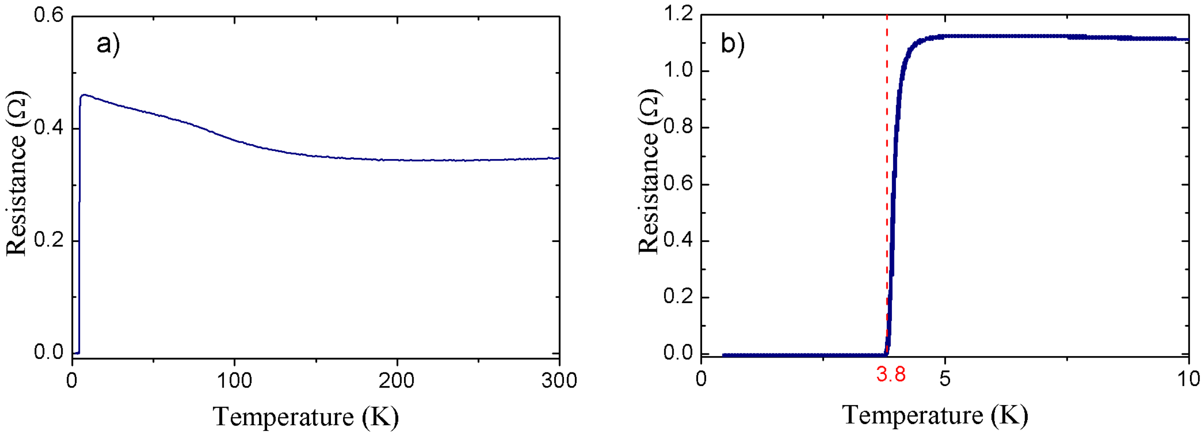

Figure 3.2: Transport experiments in BDD (a) Weak localization dominates the temperature dependence below 150 K. (b) The sample is superconducting below $T_c = 3.8$ K.

silicon (111) wafers in aqueous colloids of hydrogenated nanodiamond particles in an ultrasonic bath. Although the growth of diamond on untreated silicon results in nucleation densities of around 10^4-10^5 cm^{-2} [87], this process is known to produce nucleation densities in excess of 10^{11} cm^{-2} [88]. To acquire p-type boron doping, diamond was grown for 20 h using microwave plasma enhanced CVD (MPCVD) with 4% CH_4 diluted in H_2 with 6400 ppm of trimethylboron [33]. Microwave power of 3 kW and substrate temperature of 800 °C yields films of approximately 6 μm thickness. The Si substrate was removed using a mixture of HF and H_2SO_4. The former oxidizes Si, the latter removes SiO_2.
Figure 3.1 depicts the SEM image of our material[2]. The average diameter of the grains is 3 μm, which is consistent with the nucleation density of $\gtrapprox 10^{11}$ cm^{-2}.
Figure 3.2 shows transport measurements in our sample. Figure 3.2(a) exhibits an increase in resistivity with decreasing temperature below 150 K. Earlier reports [39, 44, 45] suggest that weak localization is responsible for this behaviour. Figure 3.2(b) indicates the onset of superconductivity at 3.8 K. Superconducting properties of similar nanocrystals of boron-doped diamond are analyzed in Ref. [11]. $T_c \approx 4$ K usually corresponds to a boron concentration of $n \approx 10^{21}$ cm^{-3} (or ~ 6000 ppm) according to the calibration established for samples prepared with chemical vapour deposition [49, 53].

In Fig. 3.3, the Raman spectrum of heavily boron-doped diamond (BDD) is depicted at $\lambda = 532$ nm.

The Raman bands around 500 cm^{-1} (denoted by BB-1 and BB-2 in Fig. 3.3), were assigned to boron dimers [52, 89, 90], to clustered boron atoms [90], and to amorphous diamond [91].

---

[2] SEM and transport measurements were performed by Soumen Mandal and Christopher Bäuerle.

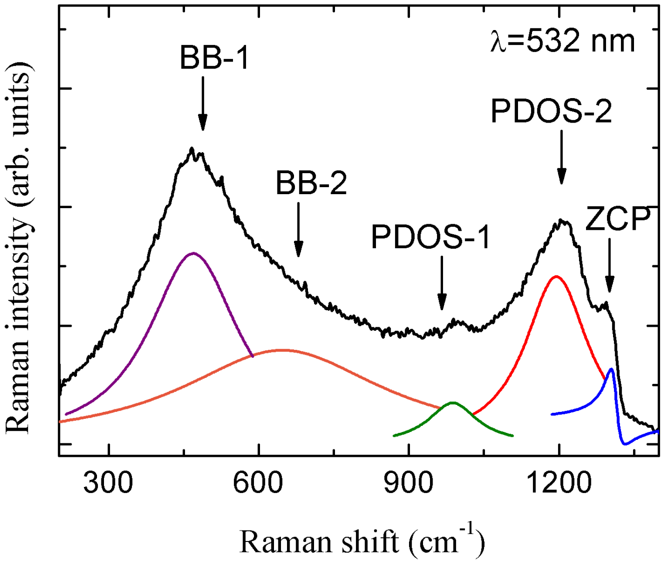

Figure 3.3: Raman spectrum of BDD at $\lambda = 532$ nm. Labels denote the boron dimers or point defect states (BB-1 and BB-2), the peaks due to the maxima of the phonon density of states (PDOS-1, PDOS-2), and the zone-center phonon line (ZCP). Solid Lorentzian (BB-1, BB-2, PDOS-1 and PDOS-2) and Fano (ZCP) lines show the fit for the spectrum.

Isotopic substitution did not give satisfying identification of the origin of the feature as both boron and carbon substitution gives shift on Raman spectra [90]. The controversy of the interpretation might be resolved by regarding boron dimers to be point defects present in BDD in high concentration. The defect concentration correlates with the incorporated boron concentration, which reaches its maximum on the surface of the nanocrystals [92]. Due to the inhomogeneous distribution of boron atoms [93], BDD does not obey the Raman wavevector conservation rule and yields similar Raman spectrum for BDD as for amorphous diamond.

The peak was fitted with the sum of two Lorentzian components (fit shown in Fig. 3.3), as opposed to a Lorentzian and a Gaussian component in Ref. [89]. The empirical relationship between the Raman shift of the lower Lorentzian component and the boron content (n) measured by secondary ion mass spectrometry (SIMS) found in Ref. [89] yields $n_{\mathrm{B}} \approx 1.8 \cdot 10^{21}$ cm^{-3} for the boron content in the sample. The approximate agreement between SIMS results and the fit further proves that the mode might be due to the high boron dimer concentration.

The Raman band around 1000 cm^{-1} (PDOS-1) originates from the maximum of the phonon density of states of diamond. As discussed above, defects in the material make the otherwise forbidden states allowed [94]. The Raman structure around 1200 cm^{-1}

consists of two components: a Lorentzian-like at 1210 cm^{-1} and another one with an asymmetric lineshape around 1300 cm^{-1}. The 1210 cm^{-1} (PDOS-2) mode appears due to the presence of defects [90, 95], or due to boron-carbon complexes [96].

The zone center optical phonon of diamond, which occurs at 1332 cm^{-1} with $\gamma = 1.2$ cm^{-1} linewidth [97], is shifted to 1300-1313 cm^{-1} in BDD and acquires a Fano lineshape due to the presence of free charge carriers [96, 98].

In Fig. 3.3, a Fano lineshape is shown fitted on the Raman spectrum. The Fano lineshape [99] originates from the quantum interference between the zone-center optical phonon and a continuum of electronic transitions around the same energy. It can be calculated as

$$\mathrm{Int}(\omega) \propto \frac{\left[q + \left(\frac{\omega - \Omega_0}{\Gamma}\right)\right]^2}{1 + \left(\frac{\omega - \Omega_0}{\Gamma}\right)^2}, \tag{3.1}$$

where Int(ω) is the intensity of the Raman signal, $\hbar\Omega_0$ and $\hbar\Gamma$ are respectively the real and imaginary parts of the self-energy in BDD after coupling between discrete phonon transition and a continuum of states. If the electronic continuum disappears, and $q \to \infty$, the Fano formula becomes the usual Lorentzian curve. The asymmetry parameter q conveys information on the Raman scattering amplitude of the decoupled phonon T_p and the electronic continuum T_e. The fit yields $q \approx -1.4$ and evidences an anomalously low value for $T_\mathrm{p}/T_\mathrm{e}$ [96, 100].

3.2 ESR spectrometer setup

ESR measurements in BDD were carried out on an X-band Bruker Elexsys E500 spectrometer[3]. Temperature in the 5-300 K temperature range is controlled by a (liquid helium) continuous flow Oxford cryostat. To present a typical setup, I will follow the path of the microwave (MW) radiation, with special care to the resonant cavity.

In Fig. 3.4, the scheme of an X-band ESR spectrometer is shown. The X-band MW radiation (~ 9.4 GHz) is generated by the MW source, a *Gunn diode*, with a power of 200 mW. The output of the diode is transmitted toward the detector using *waveguides*. The electromagnetic radiation is split up to three parts: a small portion is sent to the *frequency counter*, the second is transferred to the MW cavity, and the rest acts as a reference signal. The two latter parts reach *attenuators*, which reduce the amplitude of the signal[4].

---

[3] Laboratory of Physics of Complex Matter, École Polytechnique Fédérale de Lausanne

[4] As a side effect, the signal phase changes as well.

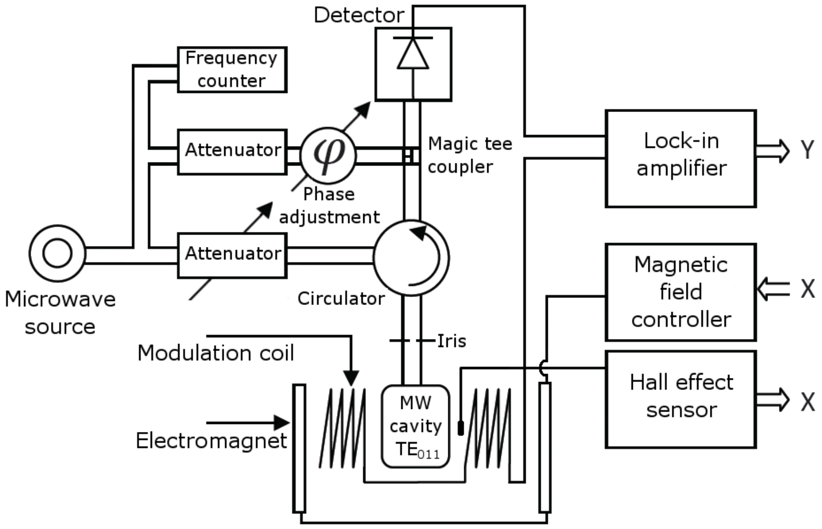

Figure 3.4: Schematic diagram of an X-band ESR spectrometer [101].[5]

The second component, i.e., the signal sent to the MW cavity, gets into the *circulator*. This multiterminal network transmits power entering the ith arm to the *(i+1)*th arm [102], thus, the power sent to and leaving the MW cavity can be transmitted through the same waveguide.

The *resonant cavity* functions as an impedance-matched load. In our cylindrical cavity, the MW cavity sustains the TE_{011} mode. This electromagnetic field configuration is the result of standing waves with no net energy flow. The dimensions of the cavity correspond to the wavelength ($\sim$ 3 cm) of the microwaves. The frequency characteristics of the resonator can be displayed by sweeping across the resonator bandwidth. If the resonant frequency is within the frequency range swept, a dip shows up on an oscilloscope. The sharpness of the response of the resonant system is described by a figure of merit, the quality factor defined by $Q = \nu/\Delta\nu$. Herein, ν is the resonance frequency and $\Delta\nu$ is the bandwidth. Differently, the Q factor can be interpreted based on the efficiency of the energy storage [103]

$$Q = 2\pi \frac{E(\text{stored in the resonator})}{E(\text{dissipated by the resonator per MW cycle})}. \tag{3.2}$$

The impedance matching of the cavity to the waveguide, which is also called the critical coupling, is found screwing a metallic partition, which extends partially across the waveguide (in a plane perpendicular to the direction of propagation): the *iris*. During the ESR

---

[5] The diagram is valid for a modified JEOL spectrometer (Department of Physics, BME). In the Bruker spectrometer, the field controller and the Hall sensor are connected to get feedback on the magnetic field value.

measurements, the load-line conditions are maintained by the *automatic frequency control* unit (AFC).

If the sample, positioned in the magnetic field maximum (B_1) in the resonant cavity, suffers an electron spin-flip, a minuscule power is reflected from the cavity. The reflected signal reads

$$\mathrm{d}E = \mathrm{d}E_0 e^{i(\omega t+\varphi)} = CB_1(\chi' - i\chi'')Ve^{i(\omega t+\varphi)} \quad (C \text{ constant}), \tag{3.3}$$

where V is the volume of the cavity. This reflection and the reference signal are summed with the *magic tee coupler* (resulting in a factor of two loss). In order that constructive interference be fulfilled, the phase of the reference arm ($E = E_0 e^{i(\omega t+\varphi_0)}$) is set with a *phase shifter* (denoted as φ in Fig. 3.4). The signal intensity at the detector diode is related to φ_0 phase as

$$I_{\text{det}} \sim |E + \mathrm{d}E|^2 = E_0^2 + 2 \cdot E_0 B_1 V \left(\chi' \cos(\varphi - \varphi_0) + \chi'' \sin(\varphi - \varphi_0)\right) + \mathcal{O}(\mathrm{d}E^2). \tag{3.4}$$

By setting $\varphi = \varphi_0 + 90°$, χ'', the dissipative answer is measured.

In an ESR experiment, the $\mathbf{B_0}$ magnetic field is swept in the *electromagnets* and the ω frequency is regarded constant in contrast to the method described in Sec. 2.3.2. Due to hysteresis, the *magnetic field controller* requires a feedback from the *Hall effect sensor.*

The signal-to-noise ratio is increased applying a *lock-in amplifier.* The radio frequency modulation, demanded by the lock-in technique, is ensured by the *modulation coils.* The frequency of the $\mathbf{B}_{\text{mod}}$ modulation is ~ 100 kHz. Then, Eq. (3.4) can be rewritten as

$$I_{\text{Lock-in}} \sim \left.\frac{\mathrm{d}I_{\text{det}}}{\mathrm{d}B}\right|_{\mathbf{B_0}} B_{\text{mod}} + \mathcal{O}(B_{\text{mod}}^2) \sim \left.\frac{\mathrm{d}\chi''}{\mathrm{d}B}\right|_{\mathbf{B_0}} V\sqrt{P}B_{\text{mod}} + \mathcal{O}(B_{\text{mod}}^2), \tag{3.5}$$

where P is the MW power. The measured ESR signal is therefore $\mathrm{d}\chi''/\mathrm{d}B$, which is a derivative Lorentzian curve (cf. Eq. (2.14) and Eq. (2.17)).

3.2.1 The Dysonian lineshape

The phenomenological Bloch equations led to a Lorentzian ESR lineshape. In contrast to our above consideration, the amplitude of the magnetic field decays exponentially in conducting materials. The characteristic length scale is the penetration depth (δ), which reads

$$\delta = \sqrt{2/\mu_0\omega\sigma}, \tag{3.6}$$

where μ_0 is the permeability of the vacuum, ω is the angular frequency of the exciting microwave, and σ is the conductivity. The time it takes to diffuse through the skin depth is T_D, which is defined by $\delta = v_{\mathrm{F}}\sqrt{\tau T_D/d}$, where v_{F} is the Fermi velocity, τ is the momentum relaxation time, and $d = 3$ is the dimensionality.

Dyson [104] showed that the lineshape in metals depends on the ratio of the skin depth (δ) to the thickness of the sample (d): $\lambda = d/\delta$. As the excited electrons can diffuse in and out of the skin depth, the ratio of T_D and the relaxation time T_1 (which is equal to T_2 in metals), $R^2 = T_D/T_1$ is also an important parameter.

In the seminal paper of Feher and Kip [105], several cases of Dyson's formula are distinguished. The relevant limit in our case (see Sec. 4.1) is $R \to \infty$ and $\lambda \to \infty$, that is, $T_T \gg T_D$ and $T_D \gg T_1$, where T_T is the time it takes for an electron to diffusively traverse the sample. With the spin-diffusion length of $\delta_{\mathrm{spin}} = v_{\mathrm{F}}\sqrt{\tau T_1/d}$, the $T_D \gg T_1$ condition is equivalent to $\delta \gg \delta_{\mathrm{spin}}$. This is "the thick plate case with slowly diffusing magnetic dipoles".

For this situation, the ESR signal can be expressed as a sum of dispersion (f^{disp}) and absorption (f^{abs}) Lorentzian lines:

$$P \propto \cos\varphi \cdot f^{\mathrm{abs}}(B - B_0, w) + \sin\varphi \cdot f^{\mathrm{disp}}(B - B_0, w), \tag{3.7}$$

where B is the magnetic field, B_0 is the resonance magnetic field, w is the linewidth, and $\varphi = 45°$.

Chapter 4

Results and discussion

In this chapter, I will present my ESR measurement results in superconducting BDD ($T_\mathrm{c} = 3.8$ K). The validity of the benchmarks of the conduction electron spin resonance signal will be analysed. I will discuss the validity of the Elliott-Yafet theory of spin relaxation in BDD.

4.1 Electron spin resonance in BDD

The critical temperature in our sample is $T_\mathrm{c} = 3.8$ K (See Sec. 3.1), thus, all measurements are performed in the normal state. Resistivity in BDD is pretty large above T_c, so the quality factor of the microwave cavity does not decrease substantially. To enhance the broad resonance signals and also to eliminate any spurious background signals from the cavity or the cryostat, one needs to employ large magnetic modulation.

The low- and high-temperature ESR measurements in BDD significantly differ. A typical low-temperature spectrum (at 35 K) is shown in Fig. 4.1(a). Due to using derivative signals in ESR (see Sec. 3.2), the signal amplitude of Lorentzian lines drops as $1/(\Delta B)^2$, where ΔB is the linewidth. Thus, the integration visually enhances the broader components [84]. In Fig. 4.1(b), the integrated spectrum is displayed confirming the presence of three different ESR signals. In the following, I refer to these as B [$g_B = 2.003(1)$], C [$g_C = 2.003(1)$], and D [$g_D = 2.016(1)$]. It is notable that B and C reveal a substantial asymmetry, whose origin will be discussed below.

Figure 4.2 illustrates the evolution of the ESR spectrum above 75 K. The intensity of the narrow line, which is the superposition of the B and C signals, decreases with increasing temperature. Nevertheless, the intensity of a broad component with resonance field $B_0 \approx 310$ mT does not change significantly.

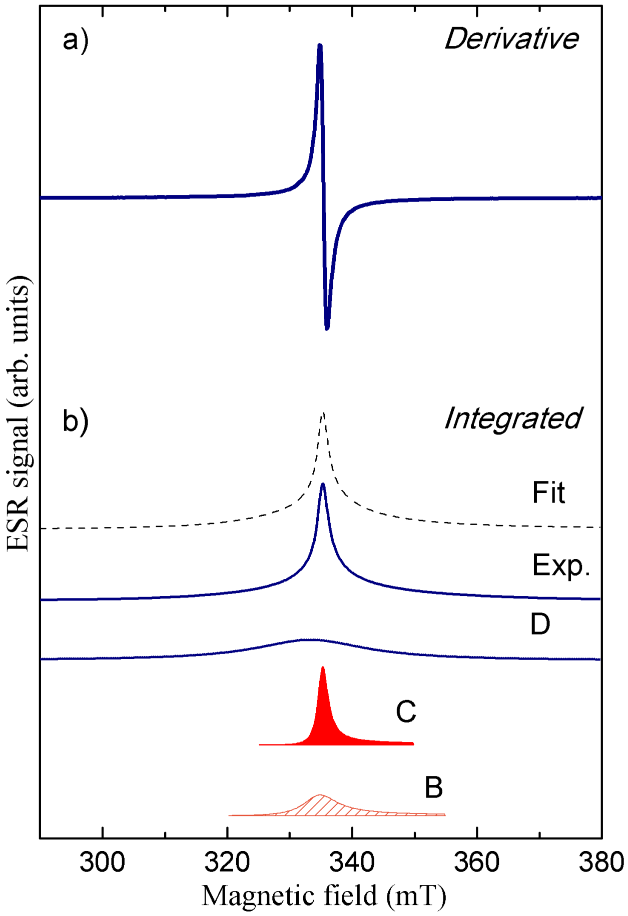

Figure 4.1: (a) The measured raw, derivative ESR spectrum of BDD at 35 K. (b) The integrated ESR spectrum (Exp.) and a fit (Fit), and the fitted components. The three components (B, C, and D lines) probably originate from carbon dangling bonds accompanying hydrogen-vacancy complexes (cf. Sec. 4.1.1). Note that the C signal is slightly asymmetric because of the finite penetration depth.

In Fig. 4.3, the derivative (Fig. 4.3(a)) and integrated (Fig. 4.3(b)) signal at 175 K is depicted in order that the broad line be more discernible. The broad component will be denoted as A [$g_A = 2.16(3)$]. The comparison of Fig. 4.1(a) and Fig. 4.2 evidences that the deconvolution of the ESR spectra into several components varies in the different temperature ranges. The D signal can be followed up to 75 K, however, starting from 75 K the fit converges to the signal A. At 75 K the two signals can be fitted independently. To prove that the A signal stems from the itinerant electrons in BDD, I will investigate the validity of the sound benchmarks distinguished in Sec. 2.3.3.

The A signal exhibits a significant asymmetry, and is best fitted with $\varphi \approx 45°$ of Eq. (3.7), which is an equal mixture of absorption and dispersion Lorentzian lines. Remarked in

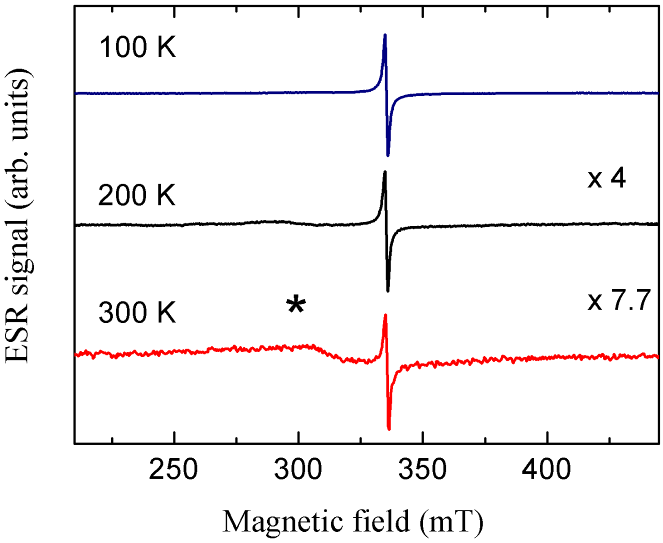

Figure 4.2: ESR spectra of BDD at different temperatures. Note the broad ESR line (denoted by asterisk) which is assigned to the conduction electrons. The sharp ESR line originates from localized defect spins.

Sec. 3.2.1, the ESR lineshape corresponds to the thick plate case. This is known as the "NMR limit" of spin diffusion of the Dysonian lineshape [105].

As I pointed out in Sec. 3.2.1, the conditions of the validity of the $\varphi \approx 45°$ case are $T_T \gg T_D$ and $T_D \gg T_1$. The latter expression is equivalent to $\delta \gg \delta_{\text{spin}}$, where δ is the penetration depth and δ_{spin} is the spin-diffusion length. Using Eq. (3.6) and room-temperature resistivity data in nanocrystalline diamond from Ref. [44], the penetration depth is estimated to be $\delta \approx 31\ \mu$m.[1] At low temperature, $\delta \approx 33\ \mu$m is calculated.

From the ESR linewidth, $T_1 \approx 0.2$ ns. With the Fermi velocity (v_{F}(BDD2) $\approx 1.1 \cdot 10^6$ m/s) and momentum relaxation time (τ(BDD2) = 5.1 fs) from an ARPES[2] study in Ref. [13], the spin-diffusion length is δ_{spin}(BDD2) $\approx 0.6\ \mu$m. These estimated values show that the condition $\delta \gg \delta_{\text{spin}}$ holds. Note that the momentum relaxation time from the Drude model yields a similar value.

Figure 4.4(a) depicts the ESR linewidth of both A and D signals as a function of temperature. The linewidth of A is 10 mT larger than that of D at $T = 75$ K. Hence, it confirms that the A and D signals have different origins. Below 75 K the A signal cannot be resolved, whose origin is unexplained. We speculate that this effect is caused by weak-localization (WL) (see Sec. 2.2.2, and Sec. 3.1), which may either lead to a sudden line

---

[1] This gives a lower bound for the penetration depth, as inter-grain interactions increase the resistivity.

[2] Angle-resolved photoemission spectroscopy

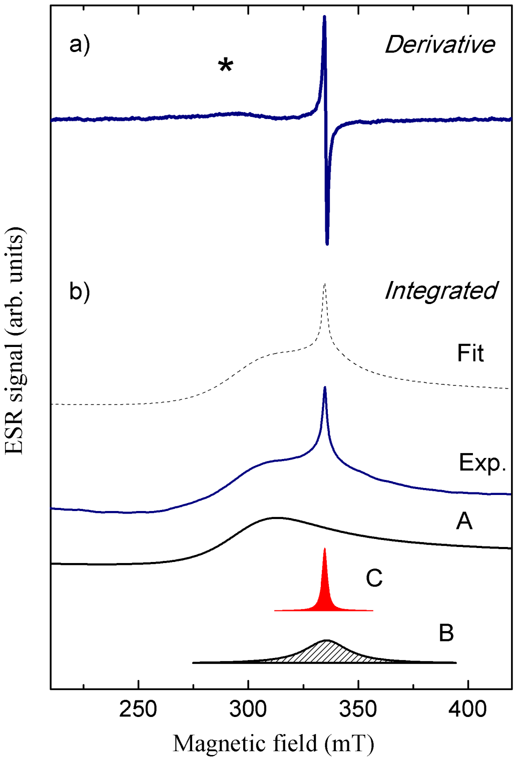

Figure 4.3: ESR spectrum of BDD at 175 K: (a) derivative signal; (b) integrated ESR signal. A fit (Fit) with three components (A, B, and C) simulates well the experiment (Exp.). Note the two narrow signals (B and C) and the broader component (A) coming from the conduction electrons.

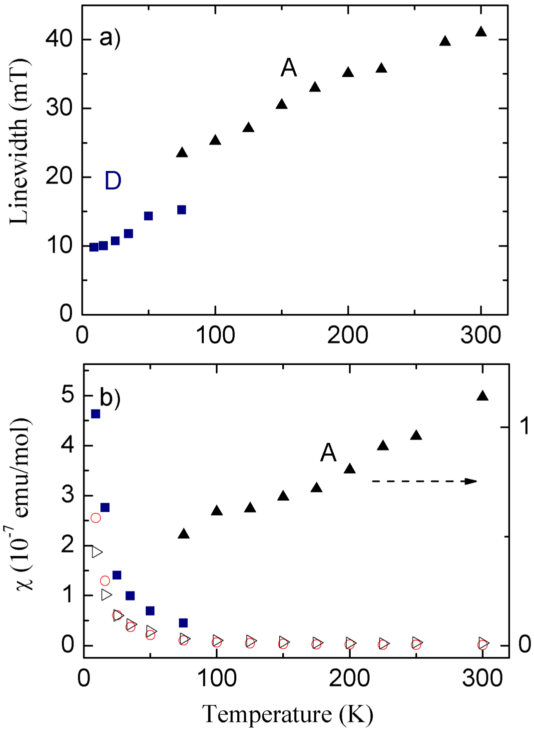

Figure 4.4: (a) ESR linewidth of the A and D ESR lines as a function of temperature. (b) Spin susceptibility as obtained from the ESR signal intensity (A: ▲, B: ▷, C: ○, and D: ■) as a function of temperature. The result for A is magnified for better visibility. Note the Curie temperature dependence for B, C, and D.

broadening or a loss of spin susceptibility. It is known that WL becomes significant in BDD below around 100-150 K [45], which supports that the change of the ESR signal of itinerant electrons and WL may be related. The linewidth of the A signal weakly increases with temperature and it has a sizable residual value. These observations are in agreement with the Elliott-Yafet theory of spin relaxation [79, 86]. In addition, the Δg is positive for BDD, which is compatible with hole nature of charge carriers in BDD [73].

In Fig. 4.4(b), the spin susceptibility of the four ESR signals are shown. B, C, and D exhibit a Curie ($\chi_{\mathrm{s}} \propto T^{-1}$, as seen in Sec. 2.3.2) temperature dependence which is characteristic for localized, paramagnetic centers. The ESR intensity of A increases by a factor two in the temperature range of 75 K to 300 K. This increase rules out that this signal would originate from localized spins. Instead, its most probable origin is the itinerant conduction electrons in BDD. A similar increase of the CESR signal intensity with a factor of

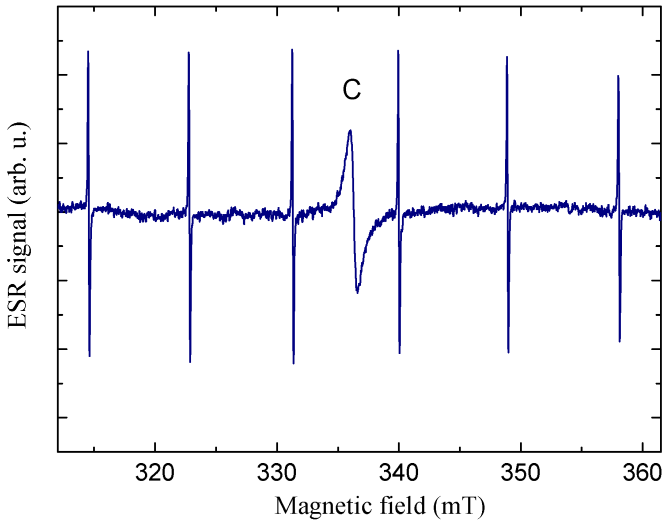

Figure 4.5: ESR spectrum of a mixture of BDD and Mn^{2+}:MgO powder at room temperature. The closely equidistant sextuplet comes from the $|-1/2\rangle \rightarrow |1/2\rangle$ Zeeman transition of Mn^{2+}. The broader central line is the C signal in BDD.

2-3 was observed in granular MgB_2 samples in the 40-300 K temperature range [71, 106]. Therein, this effect was explained by the limited microwave penetration in the metallic grains: on increasing temperature the microwave penetration depth increases due to the increasing resistivity thus resulting in an increasing CESR signal.

4.1.1 Spin susceptibility and the DOS

The ESR intensity calibration allows the measurement of the density of states at the Fermi level in metals.

ESR spectroscopy measures the net amount of magnetic moments, which is proportional to the sample amount. In order to gain information on the corresponding intensive variable, the spin susceptibility, the ESR intensity of an unknown material must be calibrated against a Curie-spin system with known amount of spins [69].

The spin susceptibilities (calculated in Eq. (2.20) and in Eq. (2.22)) are related to the ESR intensity as

$$I_{\mathrm{ESR}} \propto \sum m = B_{\mathrm{res}} \chi_s \cdot n, \tag{4.1}$$

where n is the amount of the sample and B_{res} is the magnetic field of the resonance. According to Eq. (3.5), which takes into consideration the instrumental parameters, the ESR signal intensity reads

$$I_{\mathrm{ESR}} \propto \sum m = B_{\mathrm{res}} \chi_s \cdot n \sqrt{P} B_{\mathrm{mod}}, \tag{4.2}$$

where P is the microwave power and B_{mod} is the modulation amplitude. Nevertheless, it is convenient to measure the mixture of the Curie spin system and the unknown material, thereby eliminating the instrumental parameters.

The comparison of the ESR intensity of an unknown material to a known amount of Curie spins yields

$$\frac{\chi_s(\mathrm{Unknown})}{\chi_s(\mathrm{Curie})} = \frac{I_{\mathrm{ESR}}(\mathrm{Unknown})}{I_{\mathrm{ESR}}(\mathrm{Curie})} \cdot \frac{n(\mathrm{Curie})}{n(\mathrm{Unknown})}. \tag{4.3}$$

As an example, let us assume a $S = 1/2$ Curie spin system. The ESR intensity calibration of an unknown material with itinerant electrons leads to ($g_{\mathrm{Pauli}}, g_{\mathrm{Curie}} \approx 2$)

$$\frac{I_{\mathrm{ESR}}(\mathrm{Pauli})}{I_{\mathrm{ESR}}(\mathrm{Curie})} = k_{\mathrm{B}} T D(E_{\mathrm{F}}) \frac{n(\mathrm{Pauli})}{n(\mathrm{Curie})}. \tag{4.4}$$

Eq. (4.4) can be used to determine the DOS at the Fermi energy, $D(E_{\mathrm{F}})$.

Figure 4.5 displays the ESR spectrum of mixed Mn^{2+}:MgO and BDD powder. The spectrum is a superposition of the sextuplet of Mn^{2+}:MgO ($B_{\mathrm{res}}(\mathrm{Mn}^{2+}\mathrm{:MgO}) = 336.6$ mT) and the C signal of BDD ($B_{\mathrm{res}} = 336.3$ mT).

The spin concentration of Mn^{2+}:MgO due to Mn^{2+} ions ($S = 5/2$, $L = 0$) is known to be 1.5 ppm. The only observable Zeeman transition of Mn^{2+} is $|-1/2\rangle \to |1/2\rangle$ which yields the effective $\langle S(S+1)\rangle_{\mathrm{Mn}^{2+}} = 9/4$. Eq. (2.20) gives $\chi_s(\mathrm{Mn}^{2+} : \mathrm{MgO}) = 5.63 \cdot 10^{-9}$ emu/mol for the molar spin susceptibility of Mn^{2+}:MgO. Eq. (4.3) yields $\chi_s(C) = 1.6 \cdot 10^{-7}$ emu/mol for the spin susceptibility of the C signal at room temperature.

The low modulation amplitude and low microwave power employed for the measurement in Fig. 4.5 is too low for resolving the other signals, especially the CESR (A) signal. Therefore, the spin susceptibility of the other signals in BDD is determined indirectly, i.e., the comparison of the C signal and that of A, B, and D gives the corresponding χ_s. The analysis yields $\chi_s(A) = 1.3(3) \cdot 10^{-7}$ emu/mol $= 1.1(3) \cdot 10^{-8}$ emu/g, $\chi_s(B) = 1.6(3) \cdot 10^{-7}$ emu/mol, and $\chi_s(D) = 4.8(9) \cdot 10^{-7}$ emu/mol at room temperature.

Assuming spin-1/2 paramagnetic impurities, their spin concentrations are 0.6 ppm $n_{\mathrm{imp}(C)} \approx n_{\mathrm{imp}(B)} \approx 10^{17}$ cm^{-3} and 1.8 ppm $n_{\mathrm{imp}(D)} \approx 3 \cdot 10^{17}$ cm^{-3}.

The spin concentration of the defects is in good agreement with bulk carbon dangling bond defects accompanying hydrogen-vacancy complexes found both in weakly boron-doped and as-grown CVD diamond [107, 108, 109, 110].

This accordance points to the fact that the quantity of these bulk defects mainly depends on the CH_4/H_2 ratio used for the growth of BDD [110]. The CH_4/H_2 ratio controls the grain size [111] and modifies the surface-to-bulk ratio. As the hydrogen concentration is

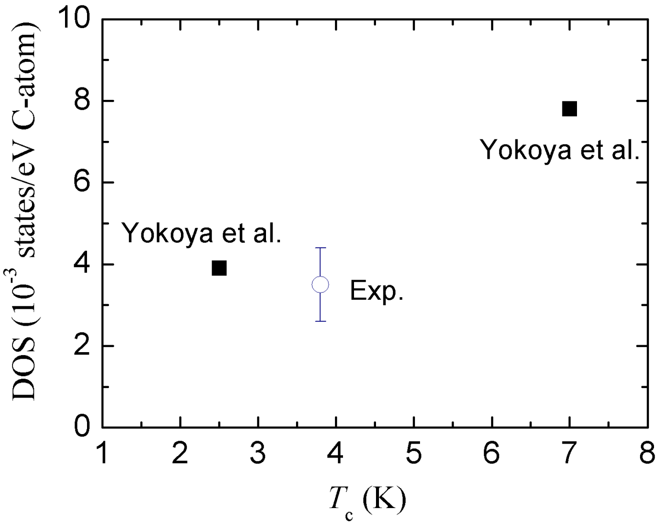

Figure 4.6: Density of electronic states in BDD versus T_c. Experimental DOS of the present work (○) is shown together with DOS calculated from the ARPES measurements in Ref. [13] (■). Error bar in our experiment is a conservative estimate and considers the uncertainty due to the limited microwave penetration depth.

higher on the grain boundaries [92], the defect concentration is expected to have a maximum there. The high concentration of defects within the penetration depth explains the asymmetry of the C signal at low temperature.

Regarding the CESR signal, the value of $\chi_s(A)$ corresponds to a DOS of $D(E_F) = 4(1)$ states/(eV·C-atom). This value is about two orders of magnitude lower spin susceptibility as compared to other metallic carbon phases such as, e.g., K_3C_{60} ($\chi_s \approx 10^{-6}$ emu/g, Ref. [112]) or the KC_8 alkali intercalated graphite $\chi_s \approx 6.4 \cdot 10^{-7}$ emu/g (Ref. [113] and Ref. [81]). This difference stems from the significantly lower carrier density in our sample ($n \approx 1.1 \cdot 10^{21}$ cm^{-3}). As an important benchmark of the CESR, the above calculated DOS value is correlated to theoretical estimates and other experimental results.

The density of states in the Fermi-gas model only depends on the free carrier concentration (n) and the band effective mass (m^*) through the Fermi wavenumber: $k_F = (3\pi^2 n)^{1/3}$. The corresponding Fermi energy is $E_F = \hbar^2 k_F^2/2m^*$. The present nominal carrier density with the free electron mass [12] corresponds to a Fermi energy of $E_F = 0.39$ eV. The DOS at the Fermi energy reads:

$$D(E_F) = \frac{1}{2\pi^2}\left(\frac{2m^*}{\hbar^2}\right)^{3/2}\sqrt{E_F}\frac{1}{\varrho}, \tag{4.5}$$

in units of states/eV · C-atom, where $\varrho = 1.76 \cdot 10^{23}$ C-atom/cm^3 is the atomic density of diamond. This gives $D(E_\mathrm{F}) = 2.4 \cdot 10^{-2}$ states/eV · C-atom.

Density functional theory (DFT) calculations[3] within the rigid band approximation were also performed (detailed in Appendix A). $n \approx 6400$ ppm boron content yields $D(E_\mathrm{F}) = 3.6 \cdot 10^{-2}$ states/(eV · C-atom).

These theoretical estimates show a significantly larger density of states. Therein, the nominal boron concentration of the MPCVD process was used, i.e., these do not take into consideration the tendency of boron dimer formation (see Sec. 3.1) [52].

In order to calculate the DOS from angle-resolved photoemission spectroscopy (ARPES) measurements [13], the Fermi surface is regarded. Within the Fermi-gas model, the density of states can be rewritten as

$$D(E_\mathrm{F}) = \frac{1}{\pi^2}\frac{k_\mathrm{F}^2}{v_\mathrm{F}\hbar}\frac{1}{\varrho}, \tag{4.6}$$

where v_F is the Fermi velocity. The given values of v_F and k_F from Ref. [13] for 'BDD2' ($T_\mathrm{c} = 2.5$ K) and 'BDD3' ($T_\mathrm{c} = 7$ K) samples give $D(E_\mathrm{F}) = 3.9 \cdot 10^{-3}$ states/(eV · C-atom) and $D(E_\mathrm{F}) = 7.8 \cdot 10^{-3}$ states/(eV · C-atom).

Figure 4.6 depicts the DOS value of our sample and those determined from ARPES measurements as a function of T_c. The empirical comparison can be justified by the BCS equation Eq. (2.1). The good agreement between the experimental values confirms the relevance of the boron dimers. In addition, the low DOS values reason the difficulty to increase T_c in BDD to the highest predicted value of 55 K [51].

4.2 Validity of the Elliott-Yafet relation

In the following, I discuss the validity of the Elliott-Yafet relation in BDD using the corrected Beuneu-Monod plot. In the original Beuneu-Monod plot [78] presented in Sec. 2.3.3, the linear scaling was established between $\Delta B/\varrho$ and $(\Delta g)^2$. Herein, a corrected scaling is used which takes into account the variation of ω_pl among metals [81], finding a linear scaling between $\Delta B/\varrho\omega_\mathrm{pl}^2$ and $(\Delta g)^2$.

In Fig. 4.7, the corrected Beuneu-Monod plot is shown together with the present results for BDD. Clearly, BDD lies out of the general trend observed for most metals. The granularity of BDD samples hinders measurement of the intrinsic ϱ [114], which leads to an overestimate of the resistivity and can contribute to the anomalous position of BDD in the Beuneu-Monod plot.

As remarked in Sec. 2.3.3, the spin relaxation in polyvalent metals like Be and Mg was

---

[3] DFT calculations were performed by János Koltai.

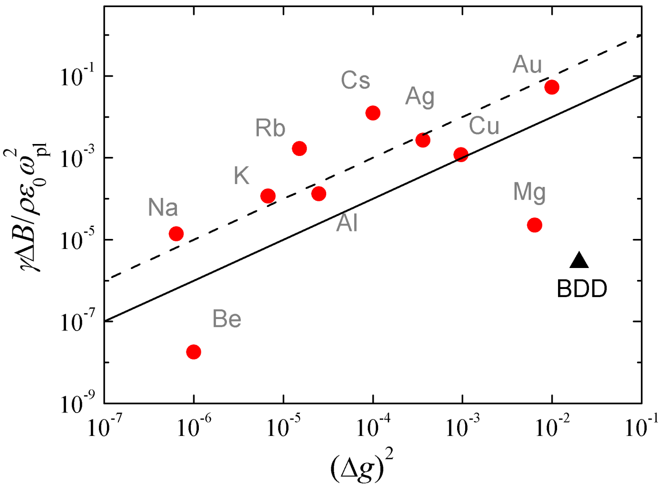

Figure 4.7: $\gamma\Delta B/\varrho\varepsilon_0\omega_{\mathrm{pl}}^2$ as a function of Δg^2 (corrected Beuneu-Monod plot [81])for elemental metals [78] (●) and BDD (▲). The resistivity data for BDD is taken from Ref. [44]. Solid and dashed lines correspond to $\alpha = 1$ and 10, respectively. We use a plasma frequency of $\omega_{\mathrm{pl}} = 0.8$ eV after Ref. [54].

explained in the “hot-spot” model [83]. The anomalously long T_1 measured in BDD might be caused by a similar effect.

Chapter 5

Summary

In this Master's thesis, I presented a summary of my Master's research project on the spin-relaxation properties of superconducting boron-doped diamond (BDD).

The thesis provides an overview of the studied material, the theory of the superconductivity in BDD, the theoretical and experimental aspects of spin dynamics in metals, the instrumentation, and the characterization of the samples.

The presented ESR measurements indicated three different paramagnetic centers with 2.2 ppm spin density. At high temperature (above 75 K), a fourth signal was identified, which is assigned to conduction electrons in BDD. The identification of the CESR signal was based on the temperature dependence of the ESR signal intensity and its absolute magnitude, which is related to the density of states at the Fermi level. The low DOS value found herein is in agreement with ARPES measurements.

The validity of the Elliott-Yafet spin-relaxation mechanism was discussed in BDD. An anomalous relationship was observed between the g-factor and the spin-relaxation time, which calls for further theoretical studies. The observed spin-relaxation rate is orders of smaller than the conventional theory predicts, which enhances the application potential of boron-doped diamond for spintronics.

My work on this project resulted in a published paper [1], a poster presentation at IWEPNM 2012, and a conference proceedings [100].

Appendix A

DFT calculations

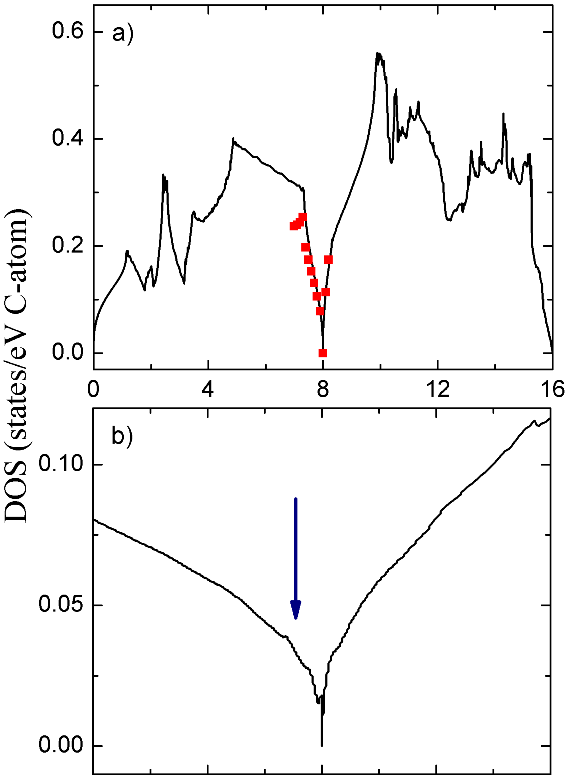

Figure A.1: Density of states calculated with DFT methods. (a) Density of states of neutral diamond as a function of number of electrons per unit cell (solid line) within LDA approximation. Density of states with optimized geometry upon adding extra charges to the system (■) (b) Zoom on the calculated DOS for neutral diamond. The charge state for our BDD sample is labeled by arrow at 7.9872.

Density functional theory calculations[1] (DFT) with the Vienna ab initio Simulation Package (VASP) [115] within the local density approximation (LDA) were also performed to calculate the density of states of neutral diamond (see Fig. A.1). The projector augmented-wave method was used with a plane-wave cutoff energy of 750 eV and a k-point set of $30\times30\times30$ Γ-centered Monkhorst-Pack grid.

A series of geometry optimization and density of states calculation with extra charges added (removed) from the system were also performed. The results are shown in Fig. A.1(a). The agreement between the DOS calculated for neutral and charged diamond firmly supports the validity of the rigid band approximation at low doping levels. The boron content of 6400 ppm yields $D(E_\mathrm{F}) = 3.6\cdot10^{-2}$ states/(eV$\cdot$C-atom) for the DOS.

---

[1] DFT calculations were performed by János Koltai.

Bibliography

[1] P. Szirmai, G. Fábián, J. Koltai, B. Náfrádi, L. Forró, T. Pichler, O. A. Williams, S. Mandal, C. Bäuerle, and F. Simon, "Observation of conduction electron spin resonance in boron-doped diamond," *Phys. Rev. B*, vol. 87, p. 195132, 2013.

[2] I. Žutić, J. Fabian, and S. D. Sarma, "Spintronics: Fundamentals and applications," *Rev. Mod. Phys.*, vol. 76, pp. 323–410, 2004.

[3] T. Jungwirth, J. Wunderlich, and K. Olejnik, "Spin Hall effect devices," *Nat. Mater.*, vol. 11, no. 5, pp. 382 – 390, 2012.

[4] J. Sinova and I. Zutic, "New moves of the spintronics tango," *Nat. Mater.*, vol. 11, no. 5, pp. 368–371, 2012.

[5] S. Zhang, "Spin Hall effect in the presence of spin diffusion," *Phys. Rev. Lett.*, vol. 85, no. 2, pp. 393 – 396, 2000.

[6] A. H. Castro Neto and F. Guinea, "Electron spin dynamics and electron spin resonance in graphene," *Eur. Phys. Lett.*, vol. 92, p. 17002, 2010.

[7] N. Tombros, C. Józsa, M. Popinciuc, H. T. Jonkman, and B. J. van Wees, "Electronic spin transport and spin precession in single graphene layers at room temperature," *Nature*, vol. 448, pp. 571–574, 2007.

[8] J. Field and J. Field, *The Properties of natural and synthetic diamond.* Academic Press, London, 1992.

[9] L. Childress, M. V. G. Dutt, J. M. Taylor, A. S. Zibrov, F. Jelezko, J. Wrachtrup, P. R. Hemmer, and M. D. Lukin, "Coherent dynamics of coupled electron and nuclear spin qubits in diamond," *Science*, vol. 314, no. 5797, pp. 281–285, 2006.

[10] G. Balasubramanian, P. Neumann, D. Twitchen, M. Markham, R. Kolesov, N. Mizuochi, J. Isoya, J. Achard, J. Beck, J. Tissler, V. Jacques, P. R. Hemmer,

F. Jelezko, and J. Wrachtrup, “Ultralong spin coherence time in isotopically engineered diamond,” *Nat. Mater.*, vol. 8, no. 5,

[11] S. Mandal, C. Naud, O. A. Williams, Étienne Bustarret, F. Omnès, P. Rodière, T. Meunier, L. Saminadayar, and C. Bäuerle, “Nanostructures made from superconducting boron-doped diamond,” *Nanotechnology*, vol. 21, no. 19, p. 195303, 2010.

[12] E. A. Ekimov, V. A. Sidorov, E. D. Bauer, N. N. Mel’nik, N. J. Curro, J. D. Thompson, and S. M. Stishov, “Superconductivity in diamond,” *Nature*, vol. 428, no. 6982, pp. 542–545, 2004.

[13] T. Yokoya, T. Nakamura, T. Matsushita, T. Muro, Y. Takano, M. Nagao, T. Takenouchi, H. Kawarada, and T. Oguchi, “Origin of the metallic properties of heavily boron-doped superconducting diamond,” *Nature*, vol. 438, no. 7068, pp. 647–650, 2005.

[14] E. Bustarret, P. Achatz, B. Sacépé, C. Chapelier, C. Marcenat, L. Ortéga, and T. Klein, “Metal-to-insulator transition and superconductivity in boron-doped diamond,” *Philos. T. Roy. Soc. A*, vol. 366, no. 1863, pp. 267–279, 2008.

[15] M. Tinkham, *Introduction to superconductivity.* Krieger Publishing Company, 1975.

[16] J. Bardeen, L. N. Cooper, and J. R. Schrieffer, “Theory of superconductivity,” *Phys. Rev.*, vol. 108, pp. 1175–1204, 1957.

[17] G. M. Éliashberg, “Interactions between electrons and lattice vibrations in a superconductor,” *Sov. Phys. JETP*, vol. 11, no. 3, pp. 966 – 976, 1960.

[18] W. L. McMillan, “Transition temperature of strong-coupled superconductors,” *Phys. Rev.*, vol. 167, pp. 331 – 344, 1968.

[19] “Wolfram Demonstrations Project. Diamond Lattice.” `http://demonstrations.wolfram.com/DiamondLattice/`. Accessed: 2013-05-27.

[20] “Element Six. Short History of the Development of CVD Diamond.” `http://www.e6cvd.com`. Accessed: 2013-05-09.

[21] L. Pan and D. Kania, *Diamond: Electronic Properties and Applications.* Kluwer Academic Publishers, 1995.

[22] P. Achatz, *Metal-insulator Transition and Superconductivity in Heavily Boron Doped Diamond and Related Materials.* PhD thesis, Université Joseph Fourier, Grenoble; Technische Universität München, 2008.

[23] Z. Teukam, J. Chevallier, C. Saguy, R. Kalish, D. Ballutaud, M. Barbe, F. Jomard, A. Tromson-Carli, C. Cytermann, J. Butler, M. Bernard, C. Baron, and A. Deneuville, "Shallow donors with high n-type electrical conductivity in homoepitaxial deuterated boron-doped diamond layers," *Nat. Mater.*, vol. 2, no. 7, pp. 482–486, 2003.

[24] J. B. Hannay, "On the artificial formation of the diamond," *Proc. Roy. Soc.*, vol. 30, pp. 188–189, 1880.

[25] F. P. Bundy, H. T. Hall, H. M. Strong, and R. H. Wentorf, "Man-made diamonds," *Nature*, vol. 176, pp. 51–55, 1955.

[26] "International Diamond Laboratories. hpht - high pressure high temperature." `http://www.diamondlab.org/80-hpht_synthesis.htm`. Accessed: 2013-05-09.

[27] A. A. Giardini and J. E. Tydings, "Diamond synthesis: Observations on the mechanism of formation," *Am. Mineral.*, vol. 47, pp. 1393–1421, 1962.

[28] P. Bachmann and R. Messier, "Emerging technology of diamond thin-films," *Chem. Eng. News*, vol. 67, no. 20, pp. 24–38, 1989.

[29] H. Kuzmany, R. Pfeiffer, N. Salk, and B. Günther, "The mystery of the 1140 cm^{-1} Raman line in nanocrystalline diamond films," *Carbon*, vol. 42, no. 5 - 6, pp. 911 – 917, 2004.

[30] J. Isberg, J. Hammersberg, E. Johansson, T. Wikström, D. J. Twitchen, A. J. Whitehead, S. E. Coe, and G. A. Scarsbrook, "High carrier mobility in single-crystal plasma-deposited diamond," *Science*, vol. 297, no. 5587, pp. 1670–1672, 2002.

[31] O. A. Williams, "Nanocrystalline diamond," *Diamond Relat. Mater.*, vol. 20, no. 5 - 6, pp. 621 – 640, 2011.

[32] P. Achatz, O. A. Williams, P. Bruno, D. M. Gruen, J. A. Garrido, and M. Stutzmann, "Effect of nitrogen on the electronic properties of ultrananocrystalline diamond thin films grown on quartz and diamond substrates," *Phys. Rev. B*, vol. 74, p. 155429, 2006.

[33] W. Gajewski, P. Achatz, O. A. Williams, K. Haenen, E. Bustarret, M. Stutzmann, and J. A. Garrido, "Electronic and optical properties of boron-doped nanocrystalline diamond films," *Phys. Rev. B*, vol. 79, p. 045206, 2009.

[34] J. R. Rabeau, A. Stacey, A. Rabeau, S. Prawer, F. Jelezko, I. Mirza, and J. Wrachtrup, "Single nitrogen vacancy centers in chemical vapor deposited diamond nanocrystals," *Nano Lett.*, vol. 7, no. 11, pp. 3433 – 3437, 2007.

[35] Y.-R. Chang, H.-Y. Lee, K. Chen, C.-C. Chang, D.-S. Tsai, C.-C. Fu, T.-S. Lim, Y.-K. Tzeng, C.-Y. Fang, C.-C. Han, H.-C. Chang, and W. Fann, "Mass production and dynamic imaging of fluorescent nanodiamonds," *Nat. Nanotechnol.*, vol. 3, no. 5, pp. 284 – 288, 2008.

[36] M. Prelas, G. Popovici, and L. Bigelow, *Handbook Of Industrial Diamonds And Diamond Films.* Marcel Dekker Incorporated, 1998.

[37] J. Kačmarčik, C. Marcenat, C. Cytermann, A. Ferreira da Silva, L. Ortega, F. Gustafsson, J. Marcus, T. Klein, E. Gheeraert, and E. Bustarret, "Superconductivity in boron-doped homoepitaxial (001)-oriented diamond layers," *Phys. Status Solidi A*, vol. 202, no. 11, pp. 2160 – 2165, 2005.

[38] N. Mott, "Conduction in glasses containing transition metal ions," *J. Non-Cryst. Solids*, vol. 1, no. 1, pp. 1 – 17, 1968.

[39] J. Mareš, M. Nesládek, P. Hubík, D. Kindl, and J. Krištofik, "On unconventional superconductivity in boron-doped diamond," *Diamond Relat. Mater.*, vol. 16, no. 1, pp. 1 – 5, 2007.

[40] J. J. Mareš, P. Hubík, M. Nesládek, and J. Kriśtofik, "Boron-doped diamond - grained mott's metal revealing superconductivity," *Diamond Relat. Mater.*, vol. 16, no. 4 - 7, pp. 921 – 925, 2007.

[41] L. Boeri, J. Kortus, and O. K. Andersen, "Three-dimensional MgB_2-type superconductivity in hole-doped diamond," *Phys. Rev. Lett.*, vol. 93, p. 237002, 2004.

[42] G. Baskaran, "Resonating valence bond mechanism of impurity band superconductivity in diamond," *J. Supercond. Nov. Magn.*, vol. 21, no. 1, pp. 45–49, 2008.

[43] J. Kortus, "Superconductivity: Where are the electrons?," *Nat. Mater.*, vol. 4, no. 12, pp. 879 – 880, 2005.

[44] J. Mareš, P. Hubík, M. Nesládek, D. Kindl, and J. Krištofik, “Weak localization - precursor of unconventional superconductivity in nanocrystalline boron-doped diamond,” *Diamond Relat. Mater.*, vol. 15, no. 11 - 12, pp. 1863 – 1867, 2006.

[45] T. Klein, P. Achatz, J. Kačmarčik, C. Marcenat, F. Gustafsson, J. Marcus, E. Bustarret, J. Pernot, F. Omnès, B. E. Sernelius, C. Persson, A. Ferreira da Silva, and C. Cytermann, “Metal-insulator transition and superconductivity in boron-doped diamond,” *Phys. Rev. B*, vol. 75, p. 165313, 2007.

[46] M. Eremets, V. Struzhkin, H. Mao, and R. Hemley, “Superconductivity in boron,” *Science*, vol. 293, no. 5528, pp. 272 – 274, 2001.

[47] N. Dubrovinskaia, R. Wirth, J. Wosnitza, T. Papageorgiou, H. F. Braun, N. Miyajima, and L. Dubrovinsky, “An insight into what superconducts in polycrystalline boron-doped diamonds based on investigations of microstructure,” *P. Natl. Acad. Sci. USA*, vol. 105, no. 33, pp. 11619 – 11622, 2008.

[48] E. Bustarret, J. Kačmarčik, C. Marcenat, E. Gheeraert, C. Cytermann, J. Marcus, and T. Klein, “Dependence of the superconducting transition temperature on the doping level in single-crystalline diamond films,” *Phys. Rev. Lett.*, vol. 93, p. 237005, 2004.

[49] Y. Takano, T. Takenouchi, S. Ishii, S. Ueda, T. Okutsu, I. Sakaguchi, H. Umezawa, H. Kawarada, and M. Tachiki, “Superconducting properties of homoepitaxial cvd diamond,” *Diamond Relat. Mater.*, vol. 16, no. 4-7, pp. 911–914, 2007.

[50] K.-W. Lee and W. E. Pickett, “Superconductivity in boron-doped diamond,” *Phys. Rev. Lett.*, vol. 93, p. 237003, 2004.

[51] J. E. Moussa and M. L. Cohen, “Constraints on T_c for superconductivity in heavily boron-doped diamond,” *Phys. Rev. B*, vol. 77, p. 064518, 2008.

[52] E. Bourgeois, E. Bustarret, P. Achatz, F. Omnès, and X. Blase, “Impurity dimers in superconducting B-doped diamond: Experiment and first-principles calculations,” *Phys. Rev. B*, vol. 74, p. 094509, 2006.

[53] H. Mukuda, T. Tsuchida, A. Harada, Y. Kitaoka, T. Takenouchi, Y. Takano, M. Nagao, I. Sakaguchi, and H. Kawarada, “11 B-NMR study in boron-doped diamond films,” *Sci. Technol. Adv. Mat.*, vol. 7, no. S1, p. S37, 2006.

[54] M. Ortolani, S. Lupi, L. Baldassarre, U. Schade, P. Calvani, Y. Takano, M. Nagao, T. Takenouchi, and H. Kawarada, "Low-energy electrodynamics of superconducting diamond," *Phys. Rev. Lett.*, vol. 97, p. 097002, 2006.

[55] N. Dubrovinskaia, L. Dubrovinsky, T. Papageorgiou, A. Bosak, M. Krisch, H. F. Braun, and J. Wosnitza, "Large carbon-isotope shift of T_c in boron-doped diamond," *Appl. Phys. Lett.*, vol. 92, no. 13, p. 132506, 2008.

[56] X. Blase, E. Bustarret, C. Chapelier, T. Klein, and C. Marcenat, "Superconducting group-IV semiconductors," *Nat. Mater.*, vol. 8, no. 5, pp. 375–382, 2009.

[57] B. Sacépé, C. Chapelier, C. Marcenat, J. Kačmarčik, T. Klein, M. Bernard, and E. Bustarret, "Tunneling spectroscopy and vortex imaging in boron-doped diamond," *Phys. Rev. Lett.*, vol. 96, p. 097006, 2006.

[58] J. M. Calleja, J. Kuhl, and M. Cardona, "Resonant Raman scattering in diamond," *Phys. Rev. B*, vol. 17, pp. 876–883, 1978.

[59] M. L. Cohen, "Superconductivity in many-valley semiconductors and in semimetals," *Phys. Rev.*, vol. 134, pp. A511–A521, 1964.

[60] E. Bustarret, C. Marcenat, P. Achatz, J. Kačmarčik, F. Lévy, A. Huxley, L. Ortega, E. Bourgeois, X. Blase, D. Débarre, and J. Boulmer, "Superconductivity in doped cubic silicon," *Nature*, vol. 444, no. 7118, pp. 465–468, 2006.

[61] Z.-A. Ren, J. Kato, T. Muranaka, J. Akimitsu, M. Kriener, and Y. Maeno, "Superconductivity in boron-doped sic," *J. Phys. Soc. Jpn.*, vol. 76, no. 10, 2007.

[62] N. Tombros, S. Tanabe, A. Veligura, C. Józsa, M. Popinciuc, H. T. Jonkman, and B. J. van Wees, "Anisotropic spin relaxation in graphene," *Phys. Rev. Lett.*, vol. 101, pp. 046601–1–4, 2008.

[63] A. Jánossy, "Resonant and nonresonant conduction-electron-spin transmission in normal metals," *Phys. Rev. B*, vol. 21, pp. 3793–3810, 1980.

[64] M. Johnson and R. H. Silsbee, "Interfacial charge-spin coupling: Injection and detection of spin magnetization in metals," *Phys. Rev. Lett.*, vol. 55, pp. 1790 – 1793, 1985.

[65] M. Johnson and R. H. Silsbee, “Coupling of electronic charge and spin at a ferromagnetic-paramagnetic metal interface,” *Phys. Rev. B*, vol. 37, pp. 5312 – 5325, 1988.

[66] M. Johnson, “Spin injection in metals and semiconductors,” *Semicond. Sci. Tech.*, vol. 17, no. 4, p. 298, 2002.

[67] F. Jedema, H. Heersche, A. Filip, J. Baselmans, and B. van Wees, “Electrical detection of spin precession in a metallic mesoscopic spin valve,” *Nature*, vol. 416, no. 6882, pp. 713 – 716, 2002.

[68] E. Zavoisky, *Paramagnetic Absorption in Perpendicular and Parallel Fields for Salts, Solutions and Metals.* PhD thesis, Kazan State University, 1944.

[69] P. Szirmai, G. Fábián, B. Dóra, J. Koltai, V. Zólyomi, J. Kürti, N. M. Nemes, L. Forró, and F. Simon, “Density of states deduced from ESR measurements on low-dimensional nanostructures; benchmarks to identify the ESR signals of graphene and SWCNTs,” *Phys. Status Solidi B*, vol. 248, no. 11, pp. 2688–2691, 2011.

[70] O. Chauvet, G. Oszlányi, L. Forró, P. Stephens, M. Tegze, G. Faigel, and A. Jánossy, “Quasi-one-dimensional electronic-structure in orthorhombic RbC_{60},” *Phys. Rev. Lett.*, vol. 72, no. 17, pp. 2721–2724, 1994.

[71] F. Simon, A. Jánossy, T. Fehér, F. Murányi, S. Garaj, L. Forró, C. Petrovic, S. L. Bud’ko, G. Lapertot, V. G. Kogan, and P. C. Canfield, “Anisotropy of superconducting MgB_2 as seen in electron spin resonance and magnetization data,” *Phys. Rev. Lett.*, vol. 87, no. 4, 2001.

[72] F. Simon, B. Dóra, F. Murányi, A. Jánossy, S. Garaj, L. Forró, S. Bud’ko, C. Petrovic, and P. C. Canfield, “Generalized Elliott-Yafet Theory of Electron Spin Relaxation in Metals: Origin of the Anomalous Electron Spin Lifetime in MgB_2,” *Phys. Rev. Lett.*, vol. 101, pp. 177003–1–4, 2008.

[73] C. P. Slichter, *Principles of Magnetic Resonance.* New York: Spinger-Verlag, 3rd ed., 1989.

[74] F. Bloch, “Nuclear induction,” *Phys. Rev.*, vol. 70, no. 7-8, pp. 460–474, 1946.

[75] J. Sólyom, *Fundamentals of the Physics of Solids Fundamentals of the Physics of Solids, Volume 1: Structure and Dynamics.* Berlin, Germany: Springer-Verlag, 2007.

[76] N. W. Ashcroft and N. D. Mermin, *Solid State Physics*. Philadelphia: Saunders College Publishing, 1976.

[77] P. Boross, B. Dóra, A. Kiss, and F. Simon, “A unified theory of the Elliott-Yafet and the D’yakonov-Perel’ spin-relaxation mechanisms,” *ArXiv e-prints*, 2012.

[78] F. Beuneu and P. Monod, “The Elliott relation in pure metals,” *Phys. Rev. B*, vol. 18, p. 2422, 1978.

[79] R. J. Elliott, “Theory of the Effect of Spin-Orbit Coupling on Magnetic Resonance in Some Semiconductors,” *Phys. Rev.*, vol. 96, pp. 266–279, 1954.

[80] Y. Yafet, “g factors and spin-lattice relaxation of conduction electrons,” in *Advances in Research and Applications* (F. Seitz and D. Turnbull, eds.), vol. 14 of *Solid State Physics*, pp. 1 – 98, Academic Press, 1963.

[81] G. Fábián, B. Dóra, A. Antal, L. Szolnoki, L. Korecz, A. Rockenbauer, N. M. Nemes, L. Forró, and F. Simon, “Testing the Elliott-Yafet spin-relaxation mechanism in KC_8: A model system of biased graphene,” *Phys. Rev. B*, vol. 85, p. 235405, 2012.

[82] P. Monod and F. Beuneu, “Conduction-electron spin flip by phonons in metals: Analysis of experimental data,” *Phys. Rev. B*, vol. 19, pp. 911–916, Jan 1979.

[83] J. Fabian and S. Das Sarma, “Spin relaxation of conduction electrons in polyvalent metals: Theory and a realistic calculation,” *Phys. Rev. Lett.*, vol. 81, no. 25, pp. 5624–5627, 1998.

[84] A. Jánossy, O. Chauvet, S. Pekker, J. R. Cooper, and L. Forró, “Conduction electron spin resonance in Rb_3C_{60},” *Phys. Rev. Lett.*, vol. 71, pp. 1091–1094, 1993.

[85] A. S. Claye, N. M. Nemes, A. Jánossy, and J. E. Fischer, “Structure and electronic properties of potassium-doped single-wall carbon nanotubes,” *Phys. Rev. B*, vol. 62, pp. 4845–4848 (R), 2000.

[86] Y. Yafet, “Conduction electron spin relaxation in the superconducting state,” *Phys. Lett. A*, vol. 98, no. 5-6, pp. 287–290, 1983.

[87] J. Robins, “Thin-film nucleation and growth kinetics,” *Appl. Surf. Sci.*, vol. 33 - 4, 1988.

[88] J. Hees, A. Kriele, and O. A. Williams, “Electrostatic self-assembly of diamond nanoparticles,” *Chem. Phys. Lett.*, vol. 509, no. 1 - 3, pp. 12 – 15, 2011.

[89] M. Bernard, C. Baron, and A. Deneuville, “About the origin of the low wave number structures of the Raman spectra of heavily boron doped diamond films,” *Diamond Relat. Mater.*, vol. 13, no. 4 - 8, pp. 896 – 899, 2004.

[90] V. Sidorov and E. Ekimov, “Superconductivity in diamond,” *Diamond Relat. Mater.*, vol. 19, no. 5 - 6, pp. 351 – 357, 2010.

[91] S. Prawer and R. Nemanich, “Raman spectroscopy of diamond and doped diamond,” *Philos. T. Roy. Soc. A*, vol. 362, no. 1824, pp. 2537–2565, 2004.

[92] C. Liao, Y. Wang, and S. Yang, “Depth profiles of boron and hydrogen in boron-doped diamond films and related performance characteristics,” *Diamond Relat. Mater.*, vol. 8, no. 7, pp. 1229 – 1233, 1999.

[93] H. Li, T. Zhang, L. Li, X. Lü, B. Li, Z. Jin, and G. Zou, “Investigation on crystalline structure, boron distribution, and residual stresses in freestanding boron-doped CVD diamond films,” *J. Cryst. Growth*, vol. 312, no. 12- 13, pp. 1986 – 1991, 2010.

[94] S. Prawer, K. Nugent, and D. Jamieson, “The Raman spectrum of amorphous diamond,” *Diamond Relat. Mater.*, vol. 7, no. 1, pp. 106 – 110, 1998.

[95] I. I. Vlasov, E. A. Ekimov, A. A. Basov, E. Goovaerts, and A. V. Zoteev, “On the origin of the Raman scattering in heavily boron-doped diamond,” *ArXiv e-prints*, 2008.

[96] F. Pruvost and A. Deneuville, “Analysis of the Fano in diamond,” *Diamond Relat. Mater.*, vol. 10, no. 3 - 7, pp. 531 – 535, 2001.

[97] M. S. Liu, L. A. Bursill, S. Prawer, and R. Beserman, “Temperature dependence of the first-order Raman phonon line of diamond,” *Phys. Rev. B*, vol. 61, pp. 3391–3395, 2000.

[98] E. Gheeraert, P. Gonon, A. Deneuville, L. Abello, and G. Lucazeau, “Effect of boron incorporation on the “quality” of MPCVD diamond films,” *Diamond Relat. Mater.*, vol. 2, no. 5 - 7, pp. 742 – 745, 1993.

[99] U. Fano, “Effects of configuration interaction on intensities and phase shifts,” *Phys. Rev.*, vol. 124, pp. 1866–1878, 1961.

[100] P. Szirmai, T. Pichler, O. A. Williams, S. Mandal, C. Bäuerle, and F. Simon, "A detailed analysis of the Raman spectra in superconducting boron doped nanocrystalline diamond," *Phys. Status Solidi B*, vol. 249, no. 12, pp. 2656–2659, 2012.

[101] G. Fábián, "Electron Spin Resonance in Graphite Intercalation Compounds," Master's thesis, Budapest University of Technology and Economics (BME), Hungary, 2011.

[102] C. P. Poole, *Electron Spin Resonance.* New York: John Wiley & Sons, 1983.

[103] J. Weil and J. Bolton, *Electron Paramagnetic Resonance: Elementary Theory and Practical Applications.* Wiley, 2007.

[104] F. J. Dyson, "Electron Spin Resonance Absorption in Metals II; Theory of Electron Diffusion and the Skin Effect," *Phys. Rev.*, vol. 98, p. 349, 1955.

[105] G. Feher and A. F. Kip, "Electron Spin Resonance Absorption in Metals. I. Experimental," *Phys. Rev.*, vol. 98, pp. 337–348, 1955.

[106] F. Simon, A. Jánossy, T. Fehér, F. Murányi, S. Garaj, L. Forró, C. Petrovic, S. Bud'ko, R. A. Ribeiro, and P. C. Canfield, "Magnetic-field-induced density of states in MgB_2: Spin susceptibility measured by conduction-electron spin resonance," *Phys. Rev. B*, vol. 72, p. 012511, 2005.

[107] X. Zhou, G. D. Watkins, K. M. McNamara Rutledge, R. P. Messmer, and S. Chawla, "Hydrogen-related defects in polycrystalline CVD diamond," *Phys. Rev. B*, vol. 54, pp. 7881–7890, 1996.

[108] N. Mizuochi, H. Watanabe, J. Isoya, H. Okushi, and S. Yamasaki, "Hydrogen-related defects in single crystalline CVD homoepitaxial diamond film studied by EPR," *Diamond Relat. Mater.*, vol. 13, no. 4 - 8, pp. 765 – 768, 2004.

[109] N. Mizuochi, M. Ogura, H. Watanabe, J. Isoya, H. Okushi, and S. Yamasaki, "EPR study of hydrogen-related defects in boron-doped p-type CVD homoepitaxial diamond films," *Diamond Relat. Mater.*, vol. 13, no. 11 - 12, pp. 2096 – 2099, 2004.

[110] N. Mizuochi, H. Watanabe, H. Okushi, S. Yamasaki, J. Niitsuma, and T. Sekiguchi, "Hydrogen-vacancy related defect in chemical vapor deposition homoepitaxial diamond films studied by electron paramagnetic resonance and cathodoluminescence," *Appl. Phys. Lett.*, vol. 88, no. 9, p. 091912, 2006.

[111] S. D. Janssens, P. Pobedinskas, J. Vacik, V. Petráková, B. Ruttens, J. D'Haen, M. Nesládek, K. Haenen, and P. Wagner, "Separation of intra- and intergranular magnetotransport properties in nanocrystalline diamond films on the metallic side of the metal-insulator transition," *New J. Phys.*, vol. 13, no. 8, p. 083008, 2011.

[112] O. Gunnarsson, "Superconductivity in fullerides," *Rev. Mod. Phys.*, vol. 69, pp. 575–606, 1997.

[113] M. S. Dresselhaus and G. Dresselhaus, "Intercalation compounds of graphite," *Adv. Phys.*, vol. 51, pp. 1–186, 2002.

[114] G. Zhang, S. D. Janssens, J. Vanacken, M. Timmermans, J. Vacík, G. W. Ataklti, W. Decelle, W. Gillijns, B. Goderis, K. Haenen, P. Wagner, and V. V. Moshchalkov, "Role of grain size in superconducting boron-doped nanocrystalline diamond thin films grown by CVD," *Phys. Rev. B*, vol. 84, p. 214517, 2011.

[115] G. Kresse and J. Furthmüller, "Efficient iterative schemes for ab initio total-energy calculations using a plane-wave basis set," *Phys. Rev. B*, vol. 54, pp. 11169 – 11186, 1996.